日本磁気学会
ISSN 2432-0250
Journal of the Magnetics Society of Japan
Electronic Journal URL: https://www.jstage.jst.go.jp/browse/msjmag

Vol.44 No.3 2020

Journal

JOURNAL OF THE MAGNETICS SOCIETY OF JAPAN

Vol.44 No.3 2020

日本磁気学会

ISSN 2432-0250

HP: http://www.magnetics.jp/ e-mail: msj@bj.wakwak.com

Electronic Journal: http://www.jstage.jst.go.jp/browse/msjmag

Journal of the Magnetics Society of Japan
Vol. 44, No. 3

Electronic Journal URL: https://www.jstage.jst.go.jp/browse/msjmag

CONTENTS

J. Magn. Soc. Jpn., **44**, 52-55 (2020)

Letter

Iron Loss and Magnetic Hysteresis Properties of Nanocrystalline Ring Core at High and Room Temperatures Under Inverter Excitation

A. Yao, R. Moriyama, and T. Hatakeyama
Department of Electrical and Computer Engineering, Toyama Prefectural University, *5180, Kurokawa, Imizu 939-0398, Japan*

This paper discusses the iron loss and magnetic hysteresis properties of a ring core of nanocrystalline magnetic materials (NMM) at room temperature (RT) and high temperature (HT) under pulse-width-modulation (PWM) inverter excitation. As in the case of the DC hysteresis loop, the coercivity of the NMM ring core at 300°C (HT) under PWM inverter excitation is larger than that at RT, mainly because of weakening of intergranular magnetic coupling at HT. In addition, in the NMM ring core, the area of the minor loops at HT increases compared with that at RT. Iron loss in the NMM core fed by the PWM inverter increases in tandem with an increase in temperature. Hysteresis loss increases dramatically in tandem with an increase in temperature for every tested case. In a low carrier frequency region, the eddy current loss at 300°C increases.

Key words: Nanocrystalline magnetic materials, high temperatures, iron loss, magnetic hysteresis property, inverter

1 Introduction

High temperature (HT) motor systems have been extensively studied[1–6]. Motors are generally driven by a pulse-width-modulation (PWM) inverter to control torque and rotational speed. PWM inverter outputs have higher harmonic components superimposed in fundamental waveforms. Many studies have reported that, due to high harmonic components, iron loss of the motor core under PWM inverter excitation increases[7–17] by 10%-50%[10] compared with sinusoidal excitation. In these researches, magnetic hysteresis loops had many minor loops. Thus, it was important to accurately measure and simulate the magnetic hysteresis and iron loss properties. Recently, we have shown that iron loss of conventional non-oriented (NO) electrical steel sheets and amorphous magnetic materials (AMM) excited by PWM inverter decreases in tandem with an increase in temperature[4,6]. Previous studies have also shown that in NO sheets and AMM, the area of minor loops in hysteresis loops diminishes as the temperature increases[4,6]. This study focuses on the temperature dependence of iron loss and the magnetic hysteresis properties of nanocrystalline magnetic materials (NMM) under PWM inverter excitation.

Recently, motor cores made of NMM[18,19] have been developed to reduce the iron loss of the motor system[15,20–22]. We have shown that the NMM motor is suitable for use in high-speed (HS) and high-frequency regions[22]. When HS motor systems are used, the magnetic properties of the motor core (magnetic materials) are affected by heat. Thus, as basic research to develop high-efficiency motors in HS and HT regions, it is necessary to accurately investigate the magnetic properties of the NMM core at HT under inverter excitation in experiments and numerical calculations.

This paper discusses the iron loss and magnetic hysteresis properties of NMM ring core at room temperature (RT) and HT under a single-phase full-bridge PWM inverter excitation. We experimentally and numerically examined the impact of temperature on iron loss and hysteresis (major and minor[4]) loops. This paper reports on hysteresis and eddy current losses of NMM ring at RT and HT under PWM inverter excitation.

2 Experimental and Numerical Methods

Figure 1 shows the configuration of the NMM ring specimen and its measurement system. The ring specimen is composed of NMM (FT-3M), cut into a ring shape by wire electric discharge machining[16]. The height, inner diameter, and outer diameter of the ring core of NMM are 7, 102, and 127 mm, respectively[4,6,16]. The space factor ξ_{sf} of the NMM ring core is approximately 87.3%. In this research, the exciting coil was wound around the ring specimen and the B-coil was used to measure the magnetic flux density. The ring specimen was set in the oven (ESPEC Corp., STH-120) to examine the impact of temperature on the iron loss and magnetic hysteresis properties[4] of NMM core under PWM inverter excitation.

To apply the PWM waveform to the NMM ring specimen, we used a single-phase PWM inverter (Myway Plus Corp., MWINV-9R122C). Our measurement system had a high-performance A/D converter (NI Corp., PXIe-5163, 14 bit, 50 MS/s), a current probe (HIOKI E.E. Corp., CT6711), and a voltage probe (Iwatsu Electric Co., Ltd., SS-320). The fundamental frequency, the dead time, and the modulation index were 50 Hz, 3.5 μs, and 0.7, respectively. The maximum magnetic flux density (B_{max}) was set to 0.8 T. The carrier frequency (f_c) was set to 1, 4, 12, or 20 kHz.

By using the magnetic flux density (B) and the magnetic field intensity (H), the iron loss (W_{ring}) of the NMM ring specimen is represented as[17]

$$W_{ring} = \frac{1}{T\rho}\int H\mathrm{d}B, \tag{1}$$

where T (= 0.02 s) denotes the period and ρ (= 7300 kg/m^3) is the density of NMM. In this research, B and H were given

as $\int Vdt/(N_2 S \xi_{sf})$ and $N_1 I/l$, respectively, where V denotes the voltage induced in the B-coil, N_2 (= 100) is the number of turns of B-coil, S (= 87.5 mm^2) is the cross-section of the NMM core, N_1 (= 100) is the number of turns in the exciting coil, I is the current flowing in the exciting coil, and l (= 0.36 m) is the magnetic path length.

By using the dynamic hysteresis model that combines the play model with the Cauer circuit[4–6, 23–28], we calculated the numerical hysteresis loops of the NMM ring under PWM inverter excitation. In our simulations, the hysteresis loops, $H(B)$, were calculated by[6, 26]

$$H(B) = H_{DC}(B) + \alpha\sigma d^2 \frac{7(B^k - B^{k-1}) + 2L' h_2^{k-1}}{84\Delta t + 2\alpha\sigma d^2 L'} + \alpha\sigma d^2 \frac{3L'(h_2^k - h_2^{k-1})}{420\Delta t}, \quad (2)$$

where σ denotes the electrical conductivity, $H_{DC}(B)$ is the DC hysteresis loops simulated by the play model, k is the step number, d (=18 μm) is the thickness of NMM, and Δt is the time division. Moreover, σ at RT and 300°C is 8.33×10^5 [29] and 7.27×10^5 S/m, respectively, which were obtained by the method of Ref.[30]. Meanwhile, α and L' and are fitting parameters. Each experimental DC hysteresis loop at RT and 300°C, as in the example shown in Fig. 2, was utilized in our numerical simulations (see Refs.[4–6, 26] for more detail).

This paper reports on hysteresis and eddy current losses of NMM ring at RT and HT under PWM inverter excitation. These hysteresis and eddy current losses were obtained based on our reported method[6] of the loss repartition between eddy current and hysteresis losses. As the loss repartition between eddy current and hysteresis losses, we performed the following three steps:

(1) Numerical iron losses were fitted to experimental results,
(2) Hysteresis loss was calculated at σ = 0 with Eq. (2) in numerical simulations, and
(3) Eddy current loss was calculated by subtracting the hysteresis loss from the total iron loss.

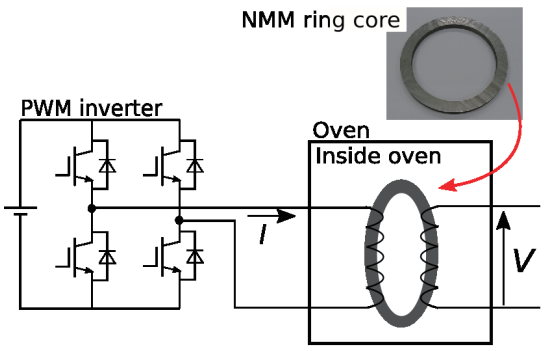

Fig. 1 NMM ring specimen and its measurement system (see Refs.[4–6, 16] for more details).

3 Results and Discussion

Figure 2 shows the DC hysteresis loops at RT and 300°C under sinusoidal excitation. In our study, the DC hysteresis loops were obtained based on the method of Ref.[26]. The NMM ring core had a hysteresis loss of 1.02 mJ/kg at RT (1.66 mJ/kg at 300°C) and at B_{max} = 0.8 T. The intergranular magnetic coupling at HT weakened and then the coercivity at HT enlarged, compared with the case at RT[31–33]. Therefore, the hysteresis loss of the NMM ring core increased in tandem with an increase in temperature.

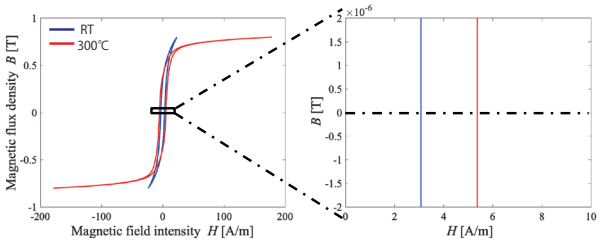

Fig. 2 Representative DC hysteresis loops of the NMM ring core at B_{max} = 0.8 T. In our numerical simulations, the DC hysteresis loops every 0.02 T were used as input (see Refs.[4–6, 26] for more detail on numerical simulations).

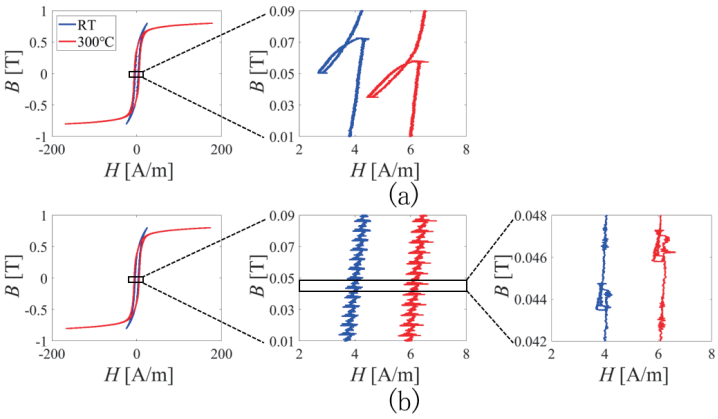

Fig. 3 Experimental hysteresis loops excited by PWM inverter, as shown in Fig. 1, at (a) f_c = 1 kHz and (b) f_c = 20 kHz.

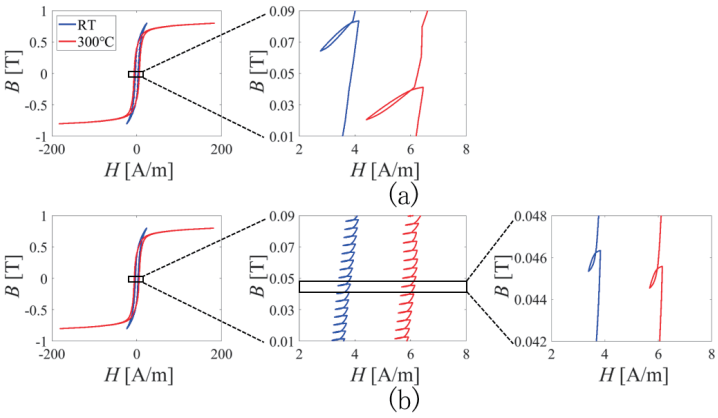

Fig. 4 Numerical hysteresis loops generated from Eq. (2) under PWM inverter excitation at (a) f_c = 1 kHz and (b) f_c = 20 kHz.

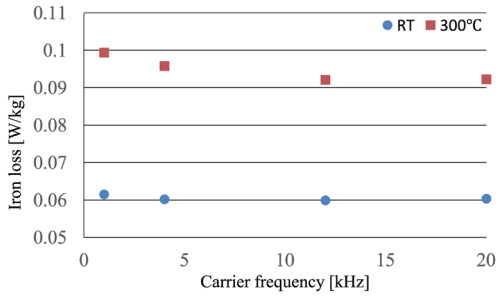

Fig. 5 Carrier frequency dependence of iron losses of NMM ring core at RT and 300°C, excited by the PWM inverter waveform.

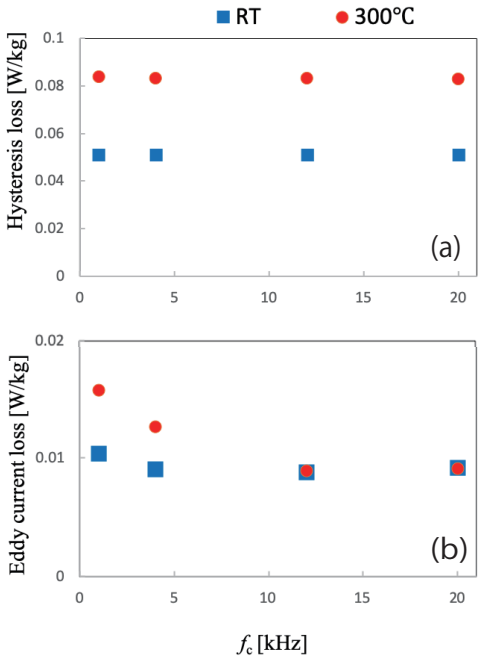

Fig. 6 (a) Hysteresis and (b) eddy current losses at different carrier frequency values.

Figure 3 shows the experimental hysteresis loops of the NMM ring core at RT and 300°C excited by the PWM inverter waveform. The carrier frequencies of Figs.(a) and (b) are 1 and 20 kHz, respectively. The iron losses at RT and 300°C are around 0.61 and 0.99 W/kg (0.60 and 0.92 W/kg) at f_c = 1 kHz (f_c = 20 kHz), respectively. The coercivity of the NMM ring core at 300°C under PWM inverter excitation is larger than that at RT, mainly because, as in the case of the DC hysteresis loop, the intergranular magnetic coupling at HT weakened. Previous studies have shown that the iron loss of NO and AMM ring cores fed by the PWM inverter decreases in tandem with an increase in temperature[4,6]. However, the iron loss of the NMM core excited by the PWM inverter increases in tandem with an increase in temperature.

The enlarged figures show that when the temperature of the NMM ring core increases, the width and the height of the minor loops increase, especially at f_c = 1 kHz. In other words, the area of the minor loop of the NMM ring core at 300°C is larger than that at RT. The area of the minor loop at RT and 300°C is 3.05 and 4.52 mW/kg (1.80 and 1.83 mW/kg) at f_c = 1 kHz (f_c = 20 kHz). Previous studies have shown that, in a ring core made of NO sheets and AMM, the area of the minor loop at HT is smaller than that at RT[4,6]. However, in the NMM ring core, the area of the minor loops at HT is greater than that at RT because H of the major loop at 300°C is greater than that at RT, as shown in Fig. 3 and then, the variation in H of the minor loop at 300°C enlarges, especially at f_c = 1 kHz. At f_c = 20 kHz, the area of the minor loop at RT and HT has almost the same values.

Figure 4 shows the hysteresis loops calculated by Eq. (2) for f_c = 1 kHz and f_c = 20 kHz. The calculated iron losses were fitted to the measured values by using the fitting parameters[5,6]. Both experimental and numerical hysteresis loops have almost the same behavior. It is considered that the slight differences between experimental and numerical loops are caused by neglecting dead time, ringing noises, and so on, in the numerical simulations[17].

Figure 5 shows the carrier frequency dependence of iron loss at RT and 300°C when the NMM ring core is excited with the inverter waveform. When the temperature of the NMM ring core increases, iron loss increases for every tested case.

Figure 6 shows the calculated hysteresis and eddy current loss at different carrier frequency values. In this research, the red and blue points showed the losses at RT and at 300°C. The hysteresis loss increased dramatically in tandem with an increase in temperature for all tested carrier frequencies. Under these experimental conditions, the ratio of hysteresis loss to total loss was high in the HT region. In a low carrier frequency region (< about 10 kHz), the eddy current loss at 300°C increased compared with that at RT, mainly because the area of the minor loop at HT was larger than that at RT, as shown in Figs. 3(a) and 4(a). In a high carrier frequency region (> about 10 kHz), the eddy current losses at RT and at 300°C had almost the same values. It is considered that, arising from the skin effect, this situation occurs mainly because the ratio of eddy current loss to the total iron loss of the NMM ring core in the high carrier frequency region is relatively low compared with that in the low carrier frequency region. Moreover, the area of the minor loop of the NMM ring core at RT and HT has almost the same values, as shown in Figs. 3(b) and 4(b). Thus, in the high carrier frequency region, an increase in total iron loss at HT depends strongly on an increase in hysteresis loss. To achieve a high-efficiency motor system at HT and HS, a design that reduces hysteresis loss and the reduction of eddy current losses by using high carrier frequencies must be considered.

4 Conclusion

For the first time, we examined the iron loss and magnetic hysteresis properties of the NMM ring core at RT and HT under a single-phase PWM inverter excitation. We confirmed that the iron loss of the NMM ring core under PWM inverter excitation

increases in tandem with an increase in temperature because of weakening of intergranular magnetic coupling at HT. Both the experiments and numerical simulations showed that the area of the minor loop of the NMM ring core at HT is larger than that at RT, especially in a low carrier frequency region. Based on experimental and numerical results, we showed that the hysteresis loss increases dramatically in tandem with an increase in temperature for all tested carrier frequencies. It was shown that the eddy current loss at 300°C increases compared with that at RT, mainly because the area of the minor loop at HT is larger than that at RT. In the future we will examine the loss ratio between major and minor loops.

Acknowledgments This work was partly supported by the JSPS KAKENHI ♯18K13749, JST OPERA ♯JPMJOP1841, JFE 21st Century Foundation, Kansai Research Foundation, Takeuchi Foundation, and Nagamori Foundation Research Grant.

References

1) L. Burdet: Ph.D. dissertation, Citeseer (2006).
2) T. D. Kefalas and A. G. Kladas: *IEEE Trans. Ind. Electron.*, **61**, 4404 (2014).
3) A. Yao, A. Adachi, and K. Fujisaki: *Proc. IEMDC*, 1 (IEEE, 2017).
4) A. Yao, S. Odawara, and K. Fujisaki: *IEEJ J. Ind. Appl.*, **7**, 298 (2018).
5) A. Yao and T. Hatakeyama: *J. Magn. Soc. Jpn.*, **43**, 46 (2019).
6) A. Yao: *J. Magn. Soc. Jpn.*, **44**, 2003L002 (2020).
7) A. Boglietti, P. Ferraris, M. Lazzari, and F. Profumo: *IEEE Trans. Magn.*, **27**, 5334 (1991).
8) A. Boglietti, P. Ferraris, M. Lazzari, and M. Pastorelli: *IEEE Trans. Magn.*, **31**, 4250 (1995).
9) M. Kawabe, T. Nomiyama, A. Shiozaki, H. Kaihara, N. Takahashi, and M. Nakano: *IEEE Trans. Magn.*, **48**, 3458 (2012).
10) K. Fujisaki and S. Liu: *J. Appl. Phys.*, **115**, 17A321 (2014).
11) A. Yao, K. Tsukada, S. Odawara, K. Fujisaki, Y. Shindo, N. Yoshikawa, and T. Yoshitake: *AIP Adv.*, **7**, 056618 (2017).
12) A. Yao and K. Fujisaki: *Proc. LDIA2017*, 1 (IEEJ, 2017).
13) A. Yao, K. Tsukada, and K. Fujisaki: *IEEJ J. Ind. Appl.*, **7**, 321 (2018).
14) A. Yao, T. Sugimoto, S. Odawara, and K. Fujisaki: *AIP Adv.*, **8**, 056804 (2018).
15) A. Yao, T. Sugimoto, S. Odawara, and K. Fujisaki: *IEEE Trans. Magn.*, **54**, 1 (2018).
16) A. Yao, T. Sugimoto, and K. Fujisaki: *IEEJ J. Ind. Appl.*, **139**, 276 (2019) (in Japanese).
17) A. Yao, T. Funaki, and T. Hatakeyama: *J. Magn. Soc. Jpn.*, **43**, 105 (2019).
18) Y. Yoshizawa and K. Yamauchi: *Mater. Trans., JIM*, **31**, 307 (1990).
19) A. Yao, M. Inoue, K. Tsukada, and K. Fujisaki: *AIP Adv.*, **8**, 056640 (2018).
20) N. Nishiyama, K. Tanimoto, and A. Makino: *AIP Adv.*, **6**, 055925 (2016).
21) N. Denis, M. Inoue, K. Fujisaki, H. Itabashi, and T. Yano: *IEEE Trans. Magn.*, **53**, 1 (2017).
22) A. Yao, T. Sugimoto, and K. Fujisaki: *J. Magn. Soc. Jpn.*, **43**, 42 (2019).
23) J. H. Krah: *IEEE Trans. Magn.*, **41**, 1444 (2005).
24) Y. Shindo and O. Noro: *IEEJ Trans. Fund. Mater.*, **134**, 173 (2014).
25) Y. Shindo, T. Miyazaki, and T. Matsuo: *IEEE Trans. Magn.*, **52**, 1 (2016).
26) S. Odawara, K. Fujisaki, T. Matsuo, and Y. Shindo: *IEEJ Trans. Ind. Appl.*, **135**, 1191 (2015).
27) T. Miyazaki, T. Mifune, T. Matsuo, Y. Shindo, Y. Takahashi, and K. Fujiwara: *J. Appl. Phys.*, **117**, 17D110 (2015).
28) S. Odawara and K. Fujisaki: *IEEE Trans. Magn.*, **54**, 1 (2018).
29) Nanocrystalline soft magnetic material catalog No. hl-fm9-h Hitachi Metals, Ltd., (in Japanese).
30) R. Moriyama, A. Yao, and T. Hatakeyama: *The papers of Technical Meeting, MAG, IEE Japan*, **MAG-19-203**, 35 (2019) (in Japanese).
31) G. Herzer: *IEEE Trans. Magn.*, **25**, 3327 (1989).
32) K. Suzuki, A. Makino, A. Inoue, and T. Masumoto: *J. Magn. Soc. Jpn.*, **18**, 800 (1994) (in Japanese).
33) K. Suzuki: *J. Magn. Soc. Jpn.*, **24**, 495 (2000) (in Japanese).

Recieved Jan. 8, 2020; Accepted Feb. 4, 2020

J. Magn. Soc. Jpn., **44**, 56-63 (2020)

<Review>

Study of spin transport and magnetoresistance effect in silicon-based lateral spin devices for spin-MOSFET applications

M. Ishikawa, Y. Saito*, and K. Hamaya**

Department of Electrical and Electronic Engineering, College of Engineering, Nihon Univ., *1 Nakagawara Tokusada, Tamura, Koriyama 963-8642, Japan*

* Center for Innovative Integrated Electronic Systems, Tohoku Univ., *468-1 Aramaki Aza Aoba, Aoba-ku, Sendai, 980-0845, Japan*

** Center for Spintronics Research Network, Graduate School of Engineering Science, Osaka Univ., *1-3 Machikaneyama, Toyonaka 560-8531, Japan*

In this paper, we introduce the current status of research and development on silicon-based spin metal-oxide-semiconductor field-effect transistors (Si spin-MOSFETs) in terms of electrical spin injection, spin transport, and spin detection in Si-based lateral spin-valve devices. First, it is important for understanding the spin transport in Si to obtain reliably large spin signals for analyses. By using n^+-Si spin-transport layers with a small cross-sectional area of ~0.3 μm^2, we can observe 50-fold the magnitude of four-terminal nonlocal (NL) magnetoresistance signals and NL Hanle signals at room temperature in previous works. Next, by analyzing these spin signals, we can reliably estimate the spin diffusion length and spin relaxation time of n^+-Si at room temperature. Also, we clarify that inter-valley spin-flip scattering is one of the dominant spin relaxation mechanisms in n^+-Si at room temperature. Furthermore, we find the crystal orientation effect on spin injection/detection efficiency in n^+-Si and discuss the possible origins. Finally, we demonstrate a room-temperature MR ratio of 0.06%, twice as large as that in the previous work.

Key-words: Si spin-MOSFETs, spin transport, spin relaxation, MR

1. Introduction

Spintronics devices typified by hard disc drive (HDD) heads and magnetic random access memories (MRAMs) contribute a lot to the storage and memory industry. From now on, spintronic technologies are expected to contribute to the future semiconductor industry. Silicon-based spin metal-oxide-semiconductor field-effect transistors (Si spin-MOSFETs) [1,2] are one of the key spintronics devices for a new logic-in-memory architecture by employing the spin degree of freedom of electrons.[2,3]

Fig. 1 shows the schematic diagram of a Si spin-MOSFET. This basic concept was proposed by Sugahara and Tanaka in 2004.[1,3] The general structure of the Si spin-MOSFET consists of a Si-MOSFET and ferromagnetic source (SO) and drain (DR) electrodes. The most important technology is the electrical spin injection and detection at SO and DR electrodes, respectively, through the spin transport in a Si channel layer. When the magnetization direction between SO/DR electrodes forms the parallel state, the current-voltage characteristics of the standard MOSFETs can usually be observed. On the other hand, when the magnetization direction between SO/DR electrodes forms the antiparallel state, the electrical resistance can be changed by depending on the spin-dependent transport in the Si spin-transport channel. This mechanism is available to utilize the magnetization state of SO/DR electrode as an enabler for bit information.[1-3] Namely, because of the integration of the two functionalities, nonvolatile memory and logic element, the Si spin-MOSFET is an innovative device for future

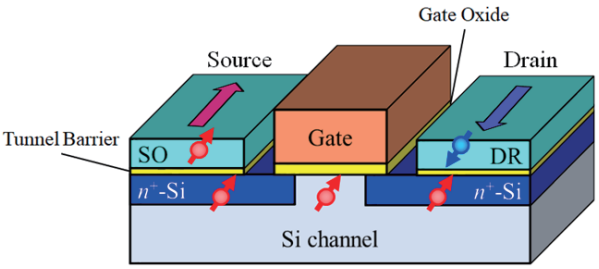

Fig. 1 (Color online) Schematic diagram of a Si spin-MOSFET with metallic source (SO) and drain (DR) structures, where SO/DR materials are ferromagnets.

semiconductor industry. It should be noted that, since the spin diffusion length of Si is relatively long (~2 μm),[4] it is possible to combine the Si spin-MOSFETs with integrated circuits.

As one of the most effective possible applications of Si spin-MOSFETs, we focus on a reconfigurable logic device.[5] A numerical benchmark for an island-style field programmable gate array (spin FPGA) using Si spin-MOSFETs has been reported by improving standard benchmark tools.[5] If the room-temperature operation of the Si spin-MOSFET with a high magnetoresistance (MR) ratio of ~100% is realized, the chip area in the spin FPGA can be significantly reduced, leading to the high speed and low-power-consumption operation.[2,5] Thus, it is important for the useful Si spin-MOSFETs to obtain a high MR ratio of ~100%.[2,5] The value of the MR ratio can be expressed as

$$\left(\frac{R_{AP}-R_P}{R_P}\right)\times 100 = \left(\frac{\Delta R}{R_P}\right)\times 100, \quad (1)$$

where R_{AP} and R_P are the resistances between SO and DR electrodes under the antiparallel and parallel states, resistively. From the one-dimensional diffusion model proposed by A. Fert *et al.* [6] and F. J. Jedema *et al.* [7], Eq. (1) in Si-based lateral spin-valve (LSV) devices can be modified as

$$\frac{|\Delta R|}{R_P} \times 100 = \frac{2(\beta r_{FM} + P r_b)^2}{A} \times 100, \quad (2)$$

$$A = \left\{ (r_b + r_{FM}) \cosh\left(\frac{d}{\lambda_{Si}}\right) + \frac{r_{Si}}{2}\left[1 + \left(\frac{r_b}{r_{Si}}\right)^2\right] \sinh\left(\frac{d}{\lambda_{Si}}\right) \right\} \left\{ 2\left(1-\beta^2\right) r_{FM} + r_{Si} \frac{d}{\lambda_{Si}} + 2\left(1-P^2\right) r_b + 2\frac{(\beta - P)^2 r_{FM} r_b + r_{Si}\left(\beta^2 r_{FM} + P^2 r_b\right) \tanh\left(\frac{d}{2\lambda_{Si}}\right)}{(r_{FM} + r_b) + r_{Si} \tanh\left(\frac{d}{2\lambda_{Si}}\right)} \right\}$$

where P is the interface spin polarization of the spin injector and detector contacts, r_b is the interface resistances between the ferromagnetic electrodes and the used Si layer, r_{FM} and r_{Si} are the spin resistance of the ferromagnetic electrode and the used Si channel layer, respectively. d is the distance between ferromagnetic electrodes, and β is the bulk spin polarization of the ferromagnet. λ_{Si} ($=\sqrt{D\tau_{Si}}$, where D and τ_{Si} are the diffusion constant and the spin lifetime, respectively) is the spin diffusion length in the used Si channel layer. From Eq. (2), we should consider that the MR ratio is influenced by several unknown parameters. If Si spin-MOSFETs with a MR ratio of ~100% were considered based on Eq. (2), we can understand that it is essential to decrease d, to enhance P, and to reduce r_b.

In this review, we introduce our recent progress of the research and development for Si spin-MOSFETs on the basis of electrical spin injection, spin transport, and spin detection in Si-based LSV devices. First, we show a reliable detection of room-temperature spin transport in Si by fabricating fine-pitch devices with a small cross-sectional area of ~0.3 μm^2. By analyzing the obtained data, reliable room-temperature spin diffusion length and spin lifetime in n^+-Si can be estimated. Next, considering the temperature dependence of the spin diffusion length and spin lifetime, we can also regard the spin relaxation mechanism in n^+-Si as a consequence of impurity- and phonon-induced inter-valley spin-flip scattering in the conduction band valleys. Furthermore, we find the crystal orientation effect on spin injection/detection efficiency in Si-based LSV devices. By combining these results, we can observe the highest MR ratio of 0.06% at room temperature. Finally, as future prospects in Si spin-MOSFETs, we propose several plans to improve the MR ratio up to 100%.

2. Current status

2.1 Spin injection and detection in Si

Since the observation of room-temperature spin accumulation signals in Si [8], lots of studies of three-terminal and four-terminal NL Hanle measurements in Si-based devices have been reported.[8-32] So far, the value of P estimated from the simple models has been discussed for Si spin-MOSFETs. Recent studies on Ge-based LSV devices [33-34] have reported that the value of P is almost the same value as the spin injection/detection efficiency estimated from NL spin transport measurements. Thus, the spin injection/detection efficiency obtained by the previous three-terminal and four-terminal NL Hanle measurements can roughly be regarded as the value of P. Fig. 2 shows the trend in the reported values of P for Si-based devices.[22-31] We find that relatively high P values have been reported year by year by using ferromagnet/MgO tunnel barrier contacts. On the other hand, the reported MR ratios measured by local two-terminal measurements were quite small less than 0.01% at room temperature,[15, 22, 24, 30, 32] largely inconsistent with the expected values from Eq. (2). This means that it is difficult to rationalize the improvement of reported P values in Fig. 2. At this stage, the precise origin of the above discrepancy in Si-based devices is still unclear. To precisely discuss the value of P as much as possible, we firstly use the small sized LSV devices for detecting reliable spin signals at room temperature.

Fig. 3 shows a typical structure of a schematic LSV device fabricated here. A channel layer consists of a Si (~70 nm) on insulator (SOI) for confining the spin transport region to the SOI layer. When the magnetization states of ferromagnetic electrodes (FM1 and FM2) can be modulated by applying external magnetic fields, the NL and local spin transport signals corresponding to the magnetization state can be observed. For this reason, the width of each FM electrode (W_{FM1} or W_{FM2}) is generally designed to be much shorter than the length of channel width (L_{CH}). However, the long length of the FM electrode may cause the suppression of the

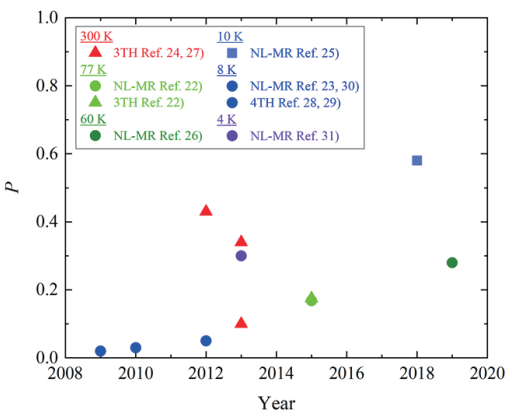

Fig. 2 (Color online) Trend in reported spin injection/detection efficiency (P) for Si-based devices.

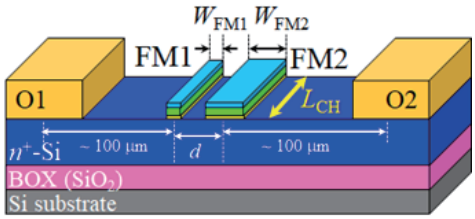

Fig. 3 (Color online) Schematic of a typical lateral spin-valve (LSV) device, consisting of two ferromagnetic electrodes (FM1 and FM2) and two nonmagnetic electrodes (O1 and O2). BOX means a buried oxide layer such as SiO_2.

magnitude of spin signals due to the large variation of the spin transport length in the Si channel region. As a result, the analytical data may include relatively large errors compared to the actual values, as indicated in Fig. 2. Thus, as mentioned above, we fabricated fine LSV devices with a small cross-sectional area of 0.305 μm² by employing a short length of L_{CH} (~7.0 μm) in the n^+-Si layer.[35] Here, we adopted CoFe and MgO as the ferromagnet and the tunnel barrier materials, respectively, because we have observed spin signals in n^+-Si by using CoFe/MgO contacts in previous studies.[12,23] In theory, Fert *et al.* have reported that thinned and fine-pitch channels in semiconductor-based LSV devices can enhance the spin signals due to the increase of the spin accumulation in semiconductors.[6,36] To obtain reliable values of spin signals, the use of the fine LSV devices is meaningful.

Fig. 4(a) shows a top-view optical micrograph of a fabricated fine LSV device. The detailed fabrication processes were reported elsewhere [35]. By using the NL terminal configuration [see Fig. 4(a)], electrical measurements were carried out using a conventional dc-bias technique at various temperatures. External magnetic fields, B_y and B_z, were applied to the directions along the in-plane and out-of-plane, respectively, for the LSV devices. Fig. 4(b) shows a representative four-terminal NL magnetoresistance signal ($\Delta R_{NL} = \Delta V_{NL}/I$) at a bias current of −1.0 mA at 303 K, where d = 1.75 μm. We can clearly see a spin-valve-like signal at room temperature. Four-terminal NL Hanle signals for the same device at 303 K are also shown in the inset of Fig. 4(b), which shows evidence for reliable spin transport in n^+-Si. It should be noted that $|\Delta R_{NL}|$ in Fig. 4(b) reaches 65 mΩ, which is approximately 50-fold the value given in Ref. 9). Therefore, we can estimate reliable room-temperature spin diffusion length and spin lifetime in n^+-Si by analyzing these reliable spin signals.

2.2 Spin diffusion length and spin lifetime in n^+-Si

In general, $|R_{NL}|$ can be expressed by the following equation [6,30,37-38]:

$$|\Delta R_{NL}| = \frac{4|P_{inj}||P_{det}|r_{Si}r_b^2\exp\left(-\frac{d}{\lambda_{Si}}\right)}{S_N\left\{(2r_b + r_{Si})^2 - r_{Si}^2\exp\left(-\frac{2d}{\lambda_{Si}}\right)\right\}}, \quad (3)$$

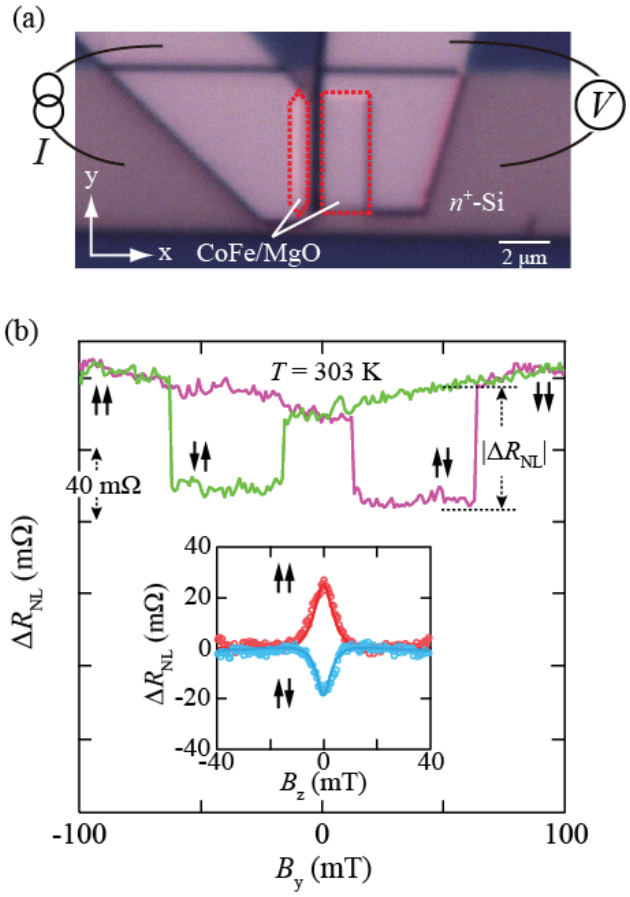

Fig. 4 (Color online) (a) Optical micrograph of fabricated n^+-Si-based LSV device. (b) Representative four-terminal nonlocal (NL) magnetoresistance curve at 303 K. Inset shows four-terminal NL Hanle-effect curves for the parallel and antiparallel magnetization configurations at 303 K. Solid curves are results of fitting to Eq. (2) in Ref. 7). Figure reprinted with permission from 35). Copyright (2016) by American Physical Society.

where P_{inj} and P_{det} are spin polarizations of the electrons in Si created by the spin injector and detector, respectively. S_N is the cross-sectional area (0.305 μm²) of the n^+-Si layer. We examined the dependence of $|\Delta R_{NL}|$ on d at 303 K in Fig. 5 [35]. Since $|\Delta R_{NL}|$ is much larger than that in previous work [8], we can observe spin signals for the LSV device with d = 3.75 μm (see inset of Fig. 5) and an exponential decay of $|\Delta R_{NL}|$ with an increase in d is seen. Using Eq. (3), we extract the room-temperature λ_{Si} of ~0.95 μm. We also extracted λ_{Si} ($= \sqrt{D\tau_{Si}}$) from the fitting of the NL Hanle-effect curves based on the one-dimensional spin drift diffusion model [6-7]. The solid curves in the inset of Fig. 4(b) show representative results of the fitting to Eq. (3) of Ref. 7). As a result, the τ_{Si} and D values at 303 K for the n^+-Si layer are estimated to be 0.7 ns and 20 cm²/s [35], respectively, leading to a λ_{Si} of 1.2 μm at 303 K, also consistent with the above framework.

Here, we summarize the reported values of λ_{Si} and τ_{Si}

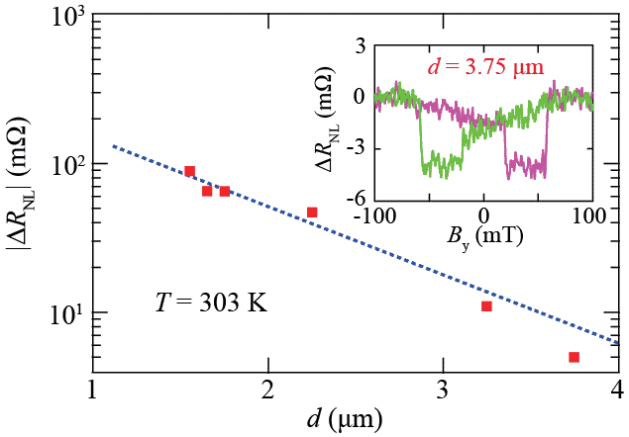

Fig. 5 (Color online) d dependence of $|\Delta R_{NL}|$ at 303 K. Dashed line shows results of fitting to Eq. (3). Inset is four-terminal NL magnetoresistance curve at 303 K for a device with d = 3.75 μm. Figure reprinted with permission from 35). Copyright (2016) by American Physical Society.

for n^+-Si with various carrier concentrations and measurement temperatures in Table 1[9,17-21,29-30,35]. There are only four experimental reports for the λ_{Si} and τ_{Si} values at room temperature. In general, to estimate the λ_{Si} and τ_{Si} values by measuring four-terminal NL magnetoresistance signals, accurate micro-fabrication processes for LSV devices with various d are necessary. If the fabricated LSV de vices have some fluctuation of the contact size and electrical characteristics, they can cause the scattering of the values of $|\Delta R_{NL}|$ for large LSV devices. Our estimated λ_{Si} values are relatively consistent with other reports in Table 1. However, we can find that the τ_{Si} values are largely different from those in Table 1. Therefore, it is important for discuss the spin relaxation mechanism in n^+-Si to use the small sized LSV devices showing large spin signals at room temperature.

2.3 Spin relaxation mechanism in n^+-Si

The spin relaxation in undoped Si has so far been discussed in terms of the Elliott-Yafet mechanism including the conduction-band valley anisotropy.[39-43] Recently, Dery and co-workers reexamined the Elliott-Yafet mechanism in multivalley semiconductors. Consequently, they predicted the detailed spin relaxation due to electron-phonon interactions in the multivalley conduction band in Si.[41-42] In addition, they also suggested donor-driven spin relaxation for doped Si.[44] This means that the conduction band dominated by the multivalley nature causes short-range spin-flip scattering due to the central-cell potential of impurities doped in Si. In the following, we simply comment on the temperature dependence of τ_{Si} in terms of these theories [41-42,44].

For all the small sized LSV devices, we measured the dependence of $|\Delta R_{NL}|$ on d at various temperatures, and then λ_{Si} as a function of temperature was obtained. Using the relation, $\lambda_{Si} = \sqrt{D\tau_{Si}}$, we can simply calculate the value of τ_{Si}. Here, we measured temperature-dependent channel mobility (μ) by using the Hall-bar device of the used n^+-Si layer (the inset of Fig. 6) and estimated the D values from the following equation [45]:

$$D = 2\left(\frac{k_B T\mu}{|q|}\right)\frac{F_{1/2}(\xi)}{F_{-1/2}(\xi)}, \quad (4)$$

Table 1 (Color online) λ_{Si} and τ_{Si} in n^+-Si estimated using various methods. NL and 4TH mean four-terminal nonlocal magnetoresistance and four-terminal nonlocal Hanle measurements, respectively. FM means material of ferromagnetic electrode used. W_{CH} means the width of the FM electrode.

Carrier density at R.T. (/cm^3)	Tunnel barrier	FM	Method	Temperature (K)	W_{CH} (μm)	λ_{Si} (μm)	τ_{Si} (nsec)	Reference
8×10^{19}	MgO/Mg	Fe	4TH	4	180	1.0 (fix)	2.0	[17]
2.7×10^{19}	MgO	Fe	4TH	10	40	2.2	18	[18]
2.7×10^{19}	MgO	Fe	4TH	300	40	1	2.5	[18]
2×10^{19}	MgO	CoFe	NL	77	100	1.6	-	[30]
1.5×10^{19}	MgO	CoFe, Co_2FeSi	4TH	20	100	0.98	4.16	[19]
1×10^{19}	MgO	Fe	4TH	8	21	2.6	9.4	[28]
1×10^{19}	MgO	Fe	NL	8	21	2.25	-	[20]
5×10^{19}	MgO	Fe	4TH	8	21	~ 2.0	10	[29]
1.8×10^{19}	MgO	Fe	4TH	8	21	2.0	10	[9]
1.8×10^{19}	MgO	Fe	4TH	300	21	~ 0.6	0.6	[9]
3×10^{18}	Al_2O_3	Fe	4TH	10	100	-	0.9	[21]
2×10^{19}	MgO	CoFe	NL	303	7	0.95	2.1	[35]
2×10^{19}	MgO	CoFe	4TH	303	7	1.2	0.7	[35]

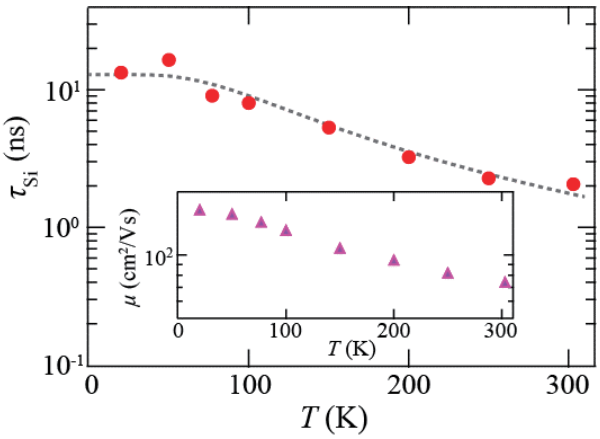

Fig. 6 (Color online) Temperature dependence of τ_{Si} in n^+-Si layer used, together with theoretical fitting curve (gray dashed curve) based on Eqs. (2)–(5) in Ref. 35). Inset shows temperature dependence of μ in the n^+-Si layer used. Figure reprinted with permission from 35). Copyright (2016) by American Physical Society.

where k_B is Boltzmann's constant, T is the temperature, q is electron's charge, and $F_n(\xi)$ is the Fermi-Dirac integral: $F_n(\xi) = \int_0^\infty x^n \, [\exp(x-\xi)+1]^{-1} dx$. The obtained temperature dependence of τ_{Si} is shown as solid symbols in Fig. 6. It should be noted that τ_{Si} is ~16 ns at low temperatures and is largely suppressed to ~2.1 ns with increasing temperature, implying the presence of strong temperature dependence. By considering Eqs. (2)–(5) in Ref. 35), we can fit the experimental data (see gray dashed curve). From the theories proposed by Dery and co-workers [41-42,44], the spin relaxation mechanism in n^+-Si is dominated by the impurity-induced spin scattering at low temperatures (T < 50 K) and the phonon-induced intervalley spin-flip scattering above 50 K,[35] respectively. We note that the temperature dependence of μ, shown in the inset of Fig. 6, also indicates the presence of the strong phonon-induced carrier scattering above 50 K. Therefore, we should regard the temperature-dependent μ for n^+-Si as an important factor for understanding the spin relaxation mechanism in n^+-Si.

2.4 Crystal orientation effect on spin injection/detection efficiency in n^+-Si

The crystal orientation effect on the spin injection in semiconductors has been discovered in (Ga,Mn)As/GaAs LSV devices.[46] That is, for epitaxial ferromagnetic (Ga,Mn)As electrodes, it is well known that there is the tunneling anisotropic spin polarization depending on the crystal orientation of GaAs.[46] After that, using three-terminal Hanle-effect measurements, similar phenomena for various ferromagnetic metal electrodes have been observed in Si.[47-48] According to the previous works on Si [47-48], the anisotropy of the tunneling spin polarization is attributed to the magnetization direction of ferromagnetic electrodes relative to the crystal orientation of Si.

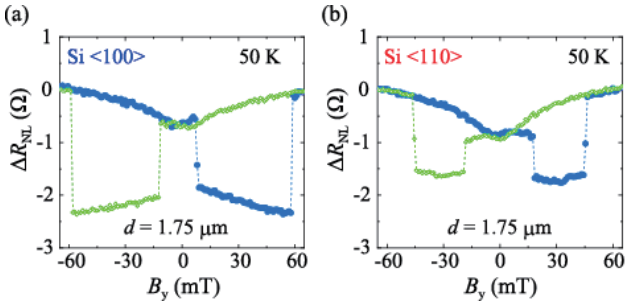

Fig. 7 (Color online) Four-terminal NL magnetoresistance curves at 50 K for (a) Si<100> and (b) Si<110> LSV devices. © IOP Publishing. Reproduced with permission. All rights reserved.

Here, we also investigated the effect of crystal orientation on the pure spin current transport in Si-LSV devices with epitaxially grown CoFe/MgO tunnel electrodes. When the crystal orientation of the spin-transport channel in LSV devices is changed from <110>, which is a conventional cleavage direction [35], to <100>, the magnitude of the spin signals is always enhanced at various conditions, as shown in Fig. 7. From the analyses based on the one-dimensional spin diffusion model, we revealed that the spin-diffusion length and spin lifetime between Si<100> and Si<110> LSV devices are comparable, while the spin injection/detection efficiency in Si<100> LSV devices is evidently larger than that in Si<110> ones. This study clarified that it is important for Si-based spintronic applications to consider the crystal orientation effect.

We infer that there are two possible origins of the difference in the spin injection/detection efficiency between Si<100> and Si<110> LSV devices.[49] One is the presence of the tunneling anisotropic spin polarization, being due to the magnetization direction of the ferromagnetic electrodes relative to the crystal orientation of semiconductors [46-48], discovered in (Ga,Mn)As/GaAs LSV devices.[46] Although the origin of the presence of the tunneling anisotropic spin polarization has not been discussed in detail [46-48], the magnetization direction of ferromagnetic electrodes relative to the crystal axis in between Si<100> and Si<110> LSV devices should also be considered. The other is the crystallographic effect of the conduction band valleys in Si. Fig. 8(c) illustrates the conduction-band valley positions in the k-space in Si; six valleys are located close to the X point along <100>. On the basis of the calculation with a full-orbital tight-binding model, similar to those in previous reports [50-51], we can roughly obtain the spin-resolved tunnel current $I_\uparrow$ and $I_\downarrow$ for a ferromagnet (FM)/MgO/Si junction.[49] Figs. 8(a) and (b) show the momentum-resolved I for spin-up (↑) and spin-down (↓), respectively. Not only the component of I around the Γ point but also that around the X point can be seen evidently in both spin states because the six conduction-band valleys are located close to the X point along <100> in the k-space in Si. That is, the tunneling spin polarization (TSP) in the FM/MgO/Si junctions can

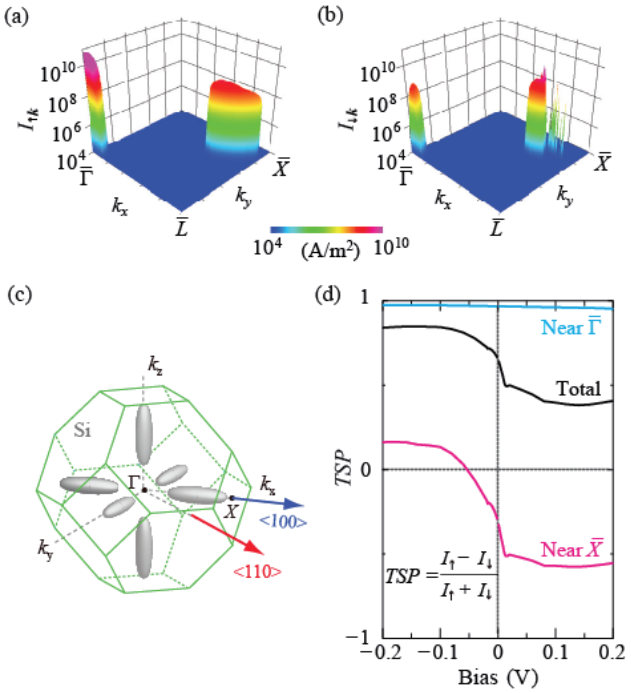

Fig. 8 (Color online) Momentum-resolved tunnel current I for (a) spin-up (↑) and (b) spin-down (↓). (c) Schematic diagram of Brillouin zone of bulk Si. (d) Calculated tunneling spin polarization (TSP) as a function of bias voltage. © IOP Publishing. Reproduced with permission. All rights reserved.

be affected by the X-point component in the electrical spin injection and detection. Fig. 8(d) presents the calculated TSP as a function of bias voltage applied to the CoFe/MgO/Si junction. Here the negative bias voltage means the condition of the spin injection from CoFe/MgO contacts into Si. The magnitude of TSP is governed by the Γ-point component in all the calculated bias conditions, but the bias-dependent behavior is evidently affected by the X-point one. From these considerations, we can expect that the conduction band valleys in Si contribute to the anisotropy of the electrical spin injection and detection through the FM/MgO/Si junctions. For enhancing the MR ratio in Si spin-MOSFETs, it is important to consider the magnetization direction of the ferromagnetic contacts relative to the Si crystal axis.

2.5 Magnetoresistance at room temperature in Si<100> devices

As described in Introduction, a large MR ratio of ~100% is required for Si spin-MOSFET applications. Finally, we discuss the two-terminal local signals ($\Delta R_{\mathrm{Local}}$) for t wo kinds of LSV devices consisting of the Si<100> or Si<110> spin-transport channel with a small size (0.305 μm^2) cross section. Fig. 9 shows a room-temperature local spin signal for a Si<100> LSV device [(a)], together with that for a Si<110> one [(b)]. Relatively

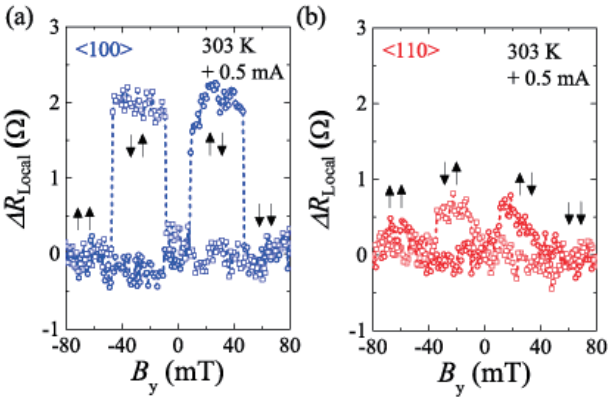

Fig. 9 (Color online) Two-terminal local-MR signals for (a) Si<100> and (b) Si<110> LSV devices at +0.5 mA (V_{bias} = 2.3 V) at room temperature. © [2018] IEEE. Reprinted, with permission, from IEEE Transactions on Magnetics.

large values of $\Delta R_{\mathrm{Local}}$ can reproducibly be observed for Si<100> LSV devices compared to those for Si<110> ones. The maximum MR ratio is 0.06% at room temperature.[52] It should be noted that this value is twice as large as that in the previous work [32]. We suggest that, for Si spin-MOSFETs with the large MR ratio, it is important to consider the crystal orientation effect described in section 2.4.

3. Future prospects for Si spin-MOSFETs

Although we have improved the MR ratio in Si-based LSV devices up to 0.06% at room temperature, there is still an enormous gap between the target value (100%) and the current value (0.06%) unfortunately. As one of the reasons, we consider that the phonon-induced spin scattering in n^+-Si influences, as discussed in section 2.3. Since the contribution of the phonon-induced intervalley spin-flip scattering was dominant as the spin relaxation in n^+-Si, we should utilize a strained-Si, which can lift the valley degeneracy of the conduction band [53-54], as a spin-transport channel to suppress the phonon-induced intervalley spin-flip scattering at room temperature.

In our opinion, the enhancement of spin injection/detection efficiency of the spin injector and detector electrodes is the most important for obtaining large MR ratios. As mentioned in section 2.1, the values of P have been scattered from device to device because of large sized LSV devices. In this study, we used small sized LSV devices and obtained values of $P < 0.2$, estimated from NL measurements. With respect to this, we will use highly ordered ferromagnetic Heusler alloys as ferromagnetic electrodes to obtain large spin polarization, as reported in previous works [55-56]. Although we have so far fabricated Co_2FeSi/MgO/Si LSV devices and observed the spin signals even at room temperature [19], the MR ratio has been still small less than 0.01%. Because of the large lattice mismatch between Co_2FeSi and MgO (~5%), the highly ordered

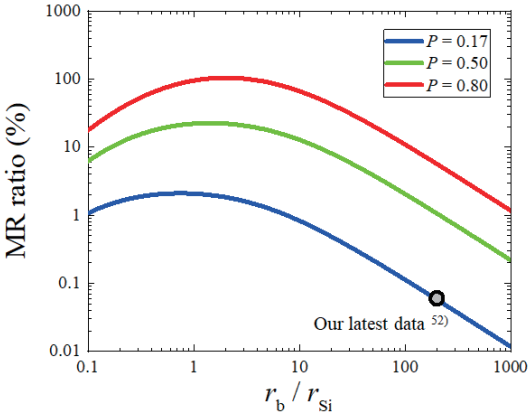

Fig. 10 (Color online) Calculated MR ratio versus r_b/r_{Si}, estimated from Eq. (2) for our fabricated fine Si-based LSV devices (d = 0.5 μm). Here, P is the spin injection/detection efficiency, r_b and r_{Si} are the spin resistance of the ferromagnet/MgO interface and the n^+-Si layer, respectively.

Co_2FeSi could not be formed for Si-based LSV devices [19]. In future, we will select highly spin-polarized Heusler alloys having a small lattice mismatch for MgO.

Finally, we will comment on the importance of reducing the interface resistance between the ferromagnetic electrodes and Si. Fig. 10 shows the dependence of the interface resistance on MR ratio estimated from the Eq. (2) [6,30,37-38], together with the maximum data we presented. When the spin injection/detection efficiency P is enhanced, one can clearly see the improvement of MR ratio. However, we have used a MgO tunnel barrier between a ferromagnet and Si. As a result, the interface resistance is so high, leading to the suppression of the MR ratio because of the large R_P in the devices. For realizing the MR ratio of ~100%, it is also important to reduce the interface resistance in addition to the enhancement of the spin injection/detection efficiency, as shown in Fig. 10. Regarding this point, we will use ferromagnet/Si Schottky tunnel contacts without using MgO. Recently, Co-based Heusler alloy/Ge Schottky tunnel contacts with a low contact resistance of less than 0.5 kΩ μm^2 were simultaneously demonstrated for Ge-based LSV devices. [56] In future, we should also explore Co-based Heusler alloy/Si Schottky tunnel contacts for high MR ratios in Si-based LSV devices.

After achieving the above three improvements, suppression of the room-temperature spin relaxation, enhancement in the spin injection/detection efficiency, and reduction in the interface resistance, a high MR ratio of 100% in Si-based LSV devices can be obtained for high-performance Si spin-MOSFETs. Therefore, we will further explore the developments of the optimum Si channel and spin injector/detector contacts in future.

4. Conclusion

Because of two functionalities, i.e., the nonvolatile memory and the logic element, Si spin-MOSFET with a MR ratio of 100% is one of the key spintronics devices for low-power-consumption Si LSI. This paper has introduced our recent progress of the development on Si spin-MOSFETs in terms of electrical spin injection, spin transport, and spin detection in Si-based LSV devices. First, by using n^+-Si spin-transport layers with a small cross-sectional area of ~0.3 μm^2, we observed 50-fold the magnitude of four-terminal NL magnetoresistance signals and NL Hanle signals at room temperature in the previous work [9]. By analyzing these spin signals, we were able to estimate the reliable spin diffusion length and spin relaxation time of n^+-Si at room temperature. Next, we clarified that the inter-valley spin-flip scattering is the dominant spin relaxation mechanism in n^+-Si at room temperature. Furthermore, we found the crystal orientation effect on spin injection/detection efficiency in n^+-Si and discussed the possible origins. From these experiments, we demonstrated a room-temperature MR ratio of 0.06%, twice as large as that in the previous work [32]. To obtain a high MR ratio of 100% in Si-based LSV devices for high-performance Si spin-MOSFETs, suppression of the room-temperature spin relaxation, enhancement in the spin injection/detection efficiency, and reduction in the interface resistance should be further explored.

Acknowledgements The author acknowledge Professor Hiroyoshi Itoh, Professor Takashi Kimura, Professor Shuta Honda, Dr. Yuichi Fujita, Dr. Michihiro Yamada, Dr. Hideyuki Sugiyama, and Dr. Tomoaki Inokuchi for useful discussions and experimental supports. This work was supported by JSPS KAKENHI Grant Number 16H02333 and 19K23522.

References

1) S. Sugahara and M. Tanaka: *Appl. Phys. Lett.*, **84**, 2307 (2004).
2) Y. Saito, T. Inokuchi, M. Ishikawa, H. Sugiyama, T. Marukame, and T. Tanamoto: *J. Elec. Chem. Soc.*, **158**, H1068 (2011).
3) M. Tanaka and S. Sugahara: *IEEE Trans. Electron Devices*, **54**, 961 (2007).
4) S. M. Thompson, D. Pugh, D. Loraine, C. L. Dennis, J. F. Gregg, C. Shirisathitkul, and W. Allen: *Spintronic Materials and Technology*, edited by Y. Xu and S. Thompson (CRC Press, USA), 249 (2006).
5) T. Tanamoto, H. Sugiyama, T. Inokuchi, T. Marukame, M. Ishikawa, K. Ikegami, and Y. Saito: *J. Appl. Phys.*, **109**, 07C312 (2011).
6) A. Fert and H. Jaffrès: *Phys. Rev. B*, **64**, 184420 (2001).
7) F. J. Jedema, H. B. Heersche, A. T. Filip, J. J. A. Baselmans, and B. J. van Wees: *Nature*, **416**, 713 (2002).
8) S. P. Dash. S. Sharma, R. S. Patel, M. P. Jong, and R. Jansen: *Nature*, **462**, 491 (2007).
9) T. Suzuki, T. Sasaki, T. Oikawa, M. Shiraishi, Y. Suzuki, and K. Noguchi: *Appl. Phys. Express*, **4**, 023003 (2011).
10) C. H. Li, O. M. J. van't Erve, and B. T. Jonker: *Nature Commum.*, **2**, 245 (2011).
11) Y. Ando, K. Kasahara, S. Yamada, Y. Maeda, K. Masaki, Y. Hoshi, K. Sawano, M. Miyao, and K. Hamaya: *Phys. Rev. B*, **85**, 035320 (2012).

12) M. Ishikawa, H. Sugiyama, T. Inokuchi, K. Hamaya, and Y. Saito: *Appl. Phys. Lett.*, **100**, 252404 (2012).
13) R. Jansen, S. P. Dash, S. Sharma, and B. C. Min: *Semicond. Sci. Technol.*, **27**, 083001 (2012).
14) H. Sugiyama, M. Ishikawa, T. Inokuchi, T. Tanamoto, Y. Saito, and N. Tezuka: *Solid State Commum.*, **190**, 46 (2014).
15) Y. Saito, T. Tanamoto, M. Ishikawa, H. Sugiyama, T. Inokuchi, K. Hamaya, and N. Tezuka: *J. Appl. Phys.*, **115**, 17C514 (2014).
16) A. Spiesser, Y. Fujita, H. Saito, S. Yamada, K. Hamaya, S. Yuasa, and R. Jansen: *Appl. Phys. Lett.*, **114**, 242401 (2019).
17) S. Sato, R. Nakane, T. Hoda, and M. Tanaka: *Phys. Rev. B*, **96**, 235204 (2017).
18) A. Spiesser, H. Saito, Y. Fujita, S. Yamada, K. Hamaya, S. Yuasa, and R. Jansen: *Phys. Rev. Appl.*, **8**, 064023 (2017).
19) M. Ishikawa, H. Sugiyama, T. Inokuchi, K. Hamaya, and Y. Saito: *Appl. Phys. Lett.*, **107**, 092402 (2015).
20) T. Sasaki, T. Oikawa, T. Suzuki, M. Shiraishi, Y. Suzuki, and K. Tagami: *Appl. Phys. Express*, **2**, 053003 (2009).
21) O. M. J. van't Erve, C. Awo-Affouda, A. T. Hanbicki, C. H. Li, P. E. Thompson, and B. T. Jonker: *IEEE Trans. Magn.*, **56**, 2343 (2009).
22) Y. Saito, M. Ishikawa, T. Inokuchi, H. Sugiyama, T. Tanamoto, K. Hamaya, and N. Tezuka: *IEEE Trans. Magn.*, **48**, 2739 (2012).
23) M. Ishikawa, H. Sugiyama, T. Inokuchi, T. Tanamoto, K. Hamaya, N. Tezuka, and Y. Saito: *J. Appl. Phys.*, **114**, 243904 (2013).
24) Y. Saito, T. Inokuchi, M. Ishikawa, T. Ajay, and H. Sugiyama: *AIP Adv.*, **7**, 055937 (2017).
25) R. Jansen, A. Spiesser, H. Saito, Y. Fujita, S. Yamada, K. Hamaya, and S. Yuasa: *Phys. Rev. Appl.*, **10**, 064050 (2018).
26) A. Spiesser, Y. Fujita, H. Saito, S. Yamada, K. Hamaya, W. Mizubayashi, K. Endo, S. Yuasa, and R. Jansen: *Phys. Rev. Appl.*, **11**, 044020 (2019).
27) A. Dankert, R. S. Dulal, and S. P. Dash: *Sci. Rep.*, **3**, 3196 (2013).
28) T. Sasaki, T. Oikawa, T. Suzuki, M. Shiraishi, Y. Suzuki, and K. Noguchi: *IEEE Trans. Magn.*, **46**, 1436 (2010).
29) M. Shiraishi, Y. Honda, E. Shikoh, Y. Suzuki, T. Shinjo, T. Sasaki, T. Oikawa, K. Noguchi, and T. Suzuki: *Phys. Rev. B*, **83**, 241204(R) (2011).
30) Y. Saito, M. Ishikawa, H. Sugiyama, T. Inokuchi, K. Hamaya, and N. Tezuka: *J. Appl. Phys.*, **117**, 17C707 (2015).
31) M. Kameno, Y. Ando, E. Shiko, T. Shinjo, T. Sasaki, T. Oikawa, Y. Suzuki, T. Suzuki, and M. Shiraishi: *Appl. Phys. Lett.*, **101**, 122413 (2012).
32) T. Sasaki, T. Suzuki, Y. Ando, H. Koike, T. Oikawa, Y. Suzuki, and M. Shiraishi: *Appl. Phys. Lett.*, **104**, 052404 (2014).
33) M. Tsukahara, M. Yamada, T. Naito, S. Yamada, K. Sawano, V. K. Lazarov, and K. Hamaya: *Appl. Phys. Express*, **12**, 033002 (2019).
34) Y. Fujita, M. Yamada, M. Tsukahara, T. Naito, S. Yamada, K. Sawano, and K. Hamaya: *Phys. Rev. B*, **100**, 024431 (2019).
35) M. Ishikawa, T. Oka, Y. Fujita, H. Sugiyama, Y. Saito, and K. Hamaya: *Phys. Rev. B*, **95**, 115302 (2017).
36) A. Fert, J.-M. George, H. Jaffrès, and R. Mattana: *IEEE Trans. Electron Devices*, **54**, 921 (2007).
37) S. Takahashi and S. Maekawa: *Phys. Rev. B*, **67**, 052409 (2003).
38) H. Jaffrès, J.-M. George, and A. Fert: *Phys. Rev. B*, **82**, 140408(R) (2001).
39) I. Appelbaum, B. Huang, and D. J. Monsma: *Nature*, **447**, 295 (2007).
40) B. Huang, D. J. Monsma, and I. Appelbaum: *Phys. Rev. Lett.*, **99**, 177209 (2007).
41) P. Li and H. Dery: *Phys. Rev. Lett.*, **107**, 107203 (2011).
42) Y. Song and H. Dery: *Phys. Rev. B*, **86**, 085201 (2012).
43) J. L. Cheng, M. W. Wu, and J. Fabian, *Phys. Rev. Lett.*, **104**, 016601 (2010).
44) Y. Song, O. Chalaev, and H. Dery: *Phys. Rev. Lett.*, **113**, 167201 (2014).
45) M. E. Flatté and J. M. Byers: *Phys. Rev. Lett.*, **84**, 4220 (2000).
46) A. Einwanger, M. Ciorga, U. Wurstbauer, D. Schuh, W. Wegscheider, and D. Weiss: *Appl. Phys. Lett.*, **95**, 152101 (2009).
47) S. Sharma, S. P. Dash, H. Saito, S. Yuasa, B. J. van Wees, and R. Jansen: *Phys. Rev. B*, **86**, 165308 (2012).
48) S. Sharma, A. Spiesser, H. Saito, S. Yuasa, B. J. van Wees, and R. Jansen: *Phys. Rev. B*, **87**, 085307 (2013).
49) M. Ishikawa, M. Tsukahara, S. Honda, Y. Fujita, M. Yamada, Y. Saito, T. Kimura, H. Itoh, and K. Hamaya: J. Phys. D: *Appl. Phys.*, **52**, 085102 (2019).
50) S. Honda, H. Itoh, J. Inoue, H. Kurebayashi, T. Trypiniotis, C. H. W. Barnes, A. Hirohata, and J. A. C. Bland: *Phys. Rev. B*, **78**, 245316 (2008).
51) S. Honda, H. Itoh, and J. Inoue: *J. Phys. D: Appl. Phys.*, **43**, 135002 (2010).
52) M. Ishikawa, M. Tsukahara, M. Yamada, Y. Saito, and K. Hamaya: *IEEE Trans. Magn.*, **54**, 1400604 (2018).
53) O. Chalaev, Y. Song, and H. Dery: *Phys. Rev. B*, **95**, 035204 (2017).
54) S. Takagi, T. Mizuno, T. Tezuka, N. Sugiyama, S. Nakaharai, T. Numata, J. Koga, and K. Uchida: *Solid-State Electron.*, **49**, 684 (2005).
55) T. Kimura, N. Hashimoto, S. Yamada, M. Miyao, and K. Hamaya: *NPG Asia Mater.*, **4**, e9 (2012).
56) K. Hamaya, Y. Fujita, M. Yamada, M. Kawano, S. Yamada, and K. Sawano: *J. Phys. D: Appl. Phys.*, **51**, 393001 (2018).

Received Jan. 07, 2020; Accepted Mar. 11, 2020

J. Magn. Soc. Jpn., **44**, 64-69 (2020)

<Paper>

Preparation of Sm–Fe–N bulk magnets with high maximum energy products

R. Matsunami, M. Matsuura, N. Tezuka, and S. Sugimoto
Department of Materials Science, Graduate School of Engineering, Tohoku Univ., *6-6-02 Aoba-yama, Sendai, 980-8579, Japan.*

In an effort to increase the maximum energy product ($(BH)_{max}$) and coercivity (H_{cJ}) of Zn-bonded Sm–Fe–N magnets, we developed a process for preparing Sm–Fe–N and Zn powders with low oxygen contents and subjected them to spark plasma sintering. The oxygen content, remanence, and coercivity of the Sm–Fe–N powder were 0.22 wt%, 151 $A \cdot m^2 \cdot kg^{-1}$, and 0.72 $MA \cdot m^{-1}$, respectively. The oxygen content and secondary average particle size of the Zn powder were 0.083 wt% and 0.93 μm, respectively. The magnetic properties of the Zn-free Sm–Fe–N magnets included an H_{cJ} of 0.86 $MA \cdot m^{-1}$ and a $(BH)_{max}$ of 188 $kJ \cdot m^{-3}$, while the Zn-bonded (10 wt%) Sm–Fe–N magnets exhibited excellent magnetic properties with a $(BH)_{max}$ of 200 $kJ \cdot m^{-3}$ and an H_{cJ} of 1.28 $MA \cdot m^{-1}$. Compared with previous studies, this is the high $(BH)_{max}$ observed for a Sm–Fe–N bulk magnet simultaneously displaying a high H_{cJ}. The $(BH)_{max}$ of the Zn-bonded magnets was greater than that of the Zn-free magnets owing to the higher relative density of the former. Therefore, Zn is an effective binder for increasing not only the coercivity but also the density of Sm–Fe–N magnets. Consequently, the procedure reported herein permits the successful preparation of high-performance Sm–Fe–N bulk magnets.

Key words: Sm–Fe–N magnets, Zn binder, maximum energy products, low oxygen content, fine Zn powder, spark plasma sintering

1. Introduction

$Sm_2Fe_{17}N_3$ is well known for its high saturation magnetization (J_s), anisotropy field (H_A), and Curie temperature (T_C). Therefore, $Sm_2Fe_{17}N_3$-based bulk magnets are expected to exhibit a high thermal stability and maximum energy product ($(BH)_{max}$). However, at temperatures exceeding 600 °C, $Sm_2Fe_{17}N_3$ decomposes into α-Fe and Sm–N. Consequently, $Sm_2Fe_{17}N_3$ powders are typically used for bonded magnets. Although resins are widely applied as the binder in bonded magnets, metal binders have also been explored. Otani et al.[1] reported that the use of Zn as the binder can increase the coercivity (H_{cJ}) of bonded magnets, which was attributed to reaction of the Zn with the soft magnetic α-Fe phase during annealing to form a non-magnetic Fe–Zn phase. As the soft magnetic α-Fe phase acts as a nucleation site for reversed magnetic domains, reducing the α-Fe phase is essential for obtaining high H_{cJ}. To improve the $(BH)_{max}$ of Sm–Fe–N magnets, it is crucial to increase the relative density and volume fraction of the Sm–Fe–N powder. Numerous researchers have tried to improve the $(BH)_{max}$ of Sm–Fe–N magnets. For example, Mashimo et al.[2] prepared Zn-free Sm–Fe–N magnets using shock compression and reported a density of 6670 $kg \cdot m^{-3}$, a $(BH)_{max}$ of 179 $kJ \cdot m^{-3}$, and a coercivity of 0.40 $MA \cdot m^{-1}$ for the resulting magnets. Ito et al.[3] prepared Zn-bonded Sm–Fe–N magnets by hot isostatic pressing and obtained a $(BH)_{max}$ and coercivity of 168 $kJ \cdot m^{-3}$ and 0.56 $MA \cdot m^{-1}$, respectively, for a 5 wt% Zn-bonded magnet. Our group has also reported Zn-bonded Sm–Fe–N magnets fabricated by mechanical processing[4,5]. Ishihara et al.[4] prepared Zn-bonded Sm–Fe–N magnets by hot-rolling and obtained a relative density of 97%, a $(BH)_{max}$ of 132 $kJ \cdot m^{-3}$, and a coercivity of 1.36 $MA \cdot m^{-1}$ for a 5 wt% Zn-bonded magnet. Kataoka et al.[5] prepared Zn-bonded Sm–Fe–N magnets by swaging and reported a $(BH)_{max}$ of 67.8 $kJ \cdot m^{-3}$, and a coercivity of 1.89 $MA \cdot m^{-1}$ for a 15 wt% Zn-bonded magnets. Furthermore, Saito[6] and Prabhu et al.[7] obtained Zn-bonded Sm–Fe–N magnets via spark plasma sintering (SPS). Saito used magnetic-field-assisted SPS to prepare 5 and 10 wt% Zn-bonded Sm–Fe–N magnets with relative densities of 88.7–92.5%. In particular, a $(BH)_{max}$ of 158 $kJ \cdot m^{-3}$ and a coercivity of 0.64 $MA \cdot m^{-1}$ were achieved for the 5 wt% Zn-bonded magnet[6]. Prabhu et al. reported a high coercivity of 2.19 $MA \cdot m^{-1}$, a high density of 6200 $kg \cdot m^{-3}$, and a $(BH)_{max}$ of approximately 70 $kJ \cdot m^{-3}$ for a 15 wt% Zn-bonded Sm–Fe–N magnet[7]. In addition, decreasing the oxygen content is important for improving the coercivity of Zn-bonded Sm–Fe–N magnets because oxygen at the surface of the Sm–Fe–N powder can decrease the coercivity[8,9] by mediating the decomposition of the $Sm_2Fe_{17}N_3$ phase. Therefore, reducing the oxygen content in Sm–Fe–N magnets suppresses the decrease in coercivity. We previously reported the preparation of high-coercivity Zn-bonded Sm–Fe–N magnets[10] using Zn powder with a low oxygen content and fine particle size, which was obtained via the hydrogen plasma–metal reaction (HPMR) method. The HPMR approach is useful for preparing fine Zn particles with a low oxygen content, and the primary and secondary average particle sizes of the obtained Zn powder were 0.23 and 0.93 μm, respectively, while the oxygen content was only 0.068 wt%[10]. The oxygen content of the Zn-bonded Sm–Fe–N magnets prepared using HPMR Zn and commercial

Sm−Fe−N powders also decreased, and high coercivities of 2.66 and 2.41 MA·m^{-1} were observed for the 15 and 10 wt% Zn-bonded Sm−Fe−N magnets, respectively. To further reduce the oxygen content of Zn-bonded Sm−Fe−N magnets, it is necessary to use a Sm−Fe−N powder with a low oxygen content. Soda et al.[11] reported that decreasing the oxygen content of the Sm−Fe−N powder was effective for suppressing the decrease in the coercivity of Sm−Fe−N bulk magnets. Recently, our group has also demonstrated that decreasing the oxygen content in $Sm_2Fe_{17}N_x$-based magnets is effective for suppressing the deterioration of coercivity during heat treatment[12]. In our previous study, Sm−Fe−N powder was synthesized without exposure to air. The resulting oxygen content was 0.23 wt%, which is one-third of that of commercial Sm−Fe−N powder. Subsequently, fine Zn particles with a diameter of several tens of nanometers were deposited on the Sm−Fe−N powder under vacuum conditions via arc plasma deposition (APD). The application of APD avoided an increase in the oxygen content of the Zn-deposited Sm−Fe−N powder, which was then subjected to sintering via SPS. The resulting 3.3 wt% Zn-bonded and Zn-free Sm−Fe−N magnets displayed $(BH)_{max}$ values of 153 and 179 kJ·m^{-3} and H_{cJ} values of 1.14 and 0.80 MA·m^{-1}, respectively[12]. Despite these promising magnetic properties obtained via a combination of APD and SPS, the APD process used for Zn deposition was complex. Thus, in this study, we investigated the use of the HPMR process to synthesize fine Zn powder with a low oxygen content and the subsequent application of this Zn powder and the Sm−Fe−N powder with low oxygen content to the fabrication of high-$(BH)_{max}$ Zn-bonded Sm−Fe−N magnets via SPS.

2. Experimental procedure

Low-oxygen-content (low-O) Sm−Fe−N powder was prepared from Sm_2Fe_{17}-based coarse Sm−Fe powder without exposure to air. The coarse Sm−Fe powder was obtained via a reduction–diffusion process and pulverized by ball milling in organic solvent with a rotational speed of 400 rpm and a milling time of 45 min. The resulting fine Sm−Fe powder was subjected to nitridation under N_2 gas at 450 °C for 25 h. Zn powder was prepared via the HPMR method with an arc current of 100 A and a hydrogen gas partial pressure of 20%. The low-O Sm−Fe−N powder and 10 wt% Zn powder were mixed via ball milling and the mixed powder was then pressed at 200 MPa under an applied magnetic field of 2.3 MA·m^{-1} in an argon atmosphere. The green compacts were subjected to SPS under a sintering pressure of 750 MPa and a sintering temperature of 300–500 °C. Zn-free Sm−Fe−N magnets were also prepared from the low-O Sm−Fe−N powder via SPS.

The magnetic properties of the Zn-free and Zn-bonded Sm−Fe−N magnets were measured using a pulsed *B*–*H* loop tracer and a DC *B*–*H* loop tracer. The magnetic properties of the raw powders were measured using a vibrating-sample magnetometer. The oxygen content was measured using an O/N analyzer, and the microstructure was examined via by field-emission scanning electron microscopy (SEM) and high-resolution transmission electron microscopy (TEM). The powder composition was determined via X-ray fluorescence. The secondary particle size distribution was measured by laser diffraction. The relative densities of the Zn-free and Zn-bonded magnets were evaluated using the reported density of $Sm_2Fe_{17}N_3$ (7.68 Mg·m^{-3})[13] and theoretical density of Zn (7.13 Mg·m^{-3}).

3. Results and discussion

The oxygen content of the low-O Sm−Fe−N powder was 0.22 wt%, which is one third of that of commercial Sm−Fe−N powder, whereas the nitrogen content was almost the same at 3.20 wt%. Figure 1 shows the particle size distribution of the low-O Sm−Fe−N powder. The average particle size (d_{50}) and d_{90}, which were evaluated from cumulative distribution, for low-O Sm−Fe−N powder were 2.47 and 5.68 μm, respectively. For comparison, the d_{50} and d_{90} of commercial powder were evaluated and these values were 2.99 and 5.26 μm, respectively. Therefore, it is suggested that the low-O Sm−Fe−N powder has smaller average particle size than commercial powder, while the low-O powder has larger amount of course powder than the commercial one. The oxygen content and secondary average particle size of the Zn powder fabricated via HPMR were evaluated, and these values were 0.083 wt% and 0.93 μm, respectively.

Figure 2 shows the hysteresis loops for the low-O and commercial Sm−Fe−N powders. The saturation magnetization and remanence of the low-O Sm−Fe−N powder were 154 A·m^2·kg^{-1} and 151 A·m^2·kg^{-1}, respectively, which were higher than those of the commercial Sm−Fe−N powder. The coercivity of the low-O Sm−Fe−N powder was 0.72 MA·m^{-1}, which was slightly less than that of the commercial Sm−Fe−N powder. The reason for the low-O Sm−Fe−N powder

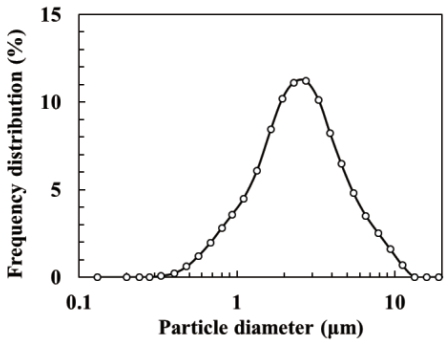

Fig. 1 Particle size distribution of the low-O Sm−Fe−N powder.

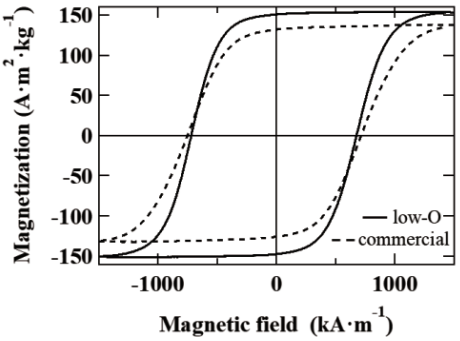

Fig. 2 Hysteresis loops for the low-O and commercial Sm–Fe–N powders.

showing slightly lower coercivity than the commercial Sm–Fe–N powder is thought that the low-O powder has coarse powders. As described above, the d_{90} of the low-O powder was larger than that of the commercial powder, therefore it can cause decrease in the coercivity. In addition, the local stray field could also decrease coercivity of the low-O Sm–Fe–N powder. The low-O Sm–Fe–N powder had angular shape because it was prepared by ball milling. The angular shape particles have high local stray field, therefore the coercivity of the low-O powder could be slightly less than that of commercial one.

After mixing the low-O Sm–Fe–N and Zn powders, the oxygen content of the mixed Sm–Fe–N/Zn powder was 0.27 wt%, corresponding to an increase in the oxygen content during the mixing process of only 0.05 wt%. The saturation magnetization and Zn content of the mixed Sm–Fe–N/Zn powder were 140 A·m^2·kg^{-1} and 10.4 wt%, respectively. The decrease in the saturation magnetization corresponds to the amount of Zn addition. Next, the mixed Sm–Fe–N/Zn powder was subjected to SPS to prepare Zn-bonded Sm–Fe–N magnets. Figure 3 presents the coercivity and $(BH)_{max}$ values of the Zn-free and Zn-bonded Sm–Fe–N magnets as functions of the sintering temperature. As shown in Fig. 3(a), the coercivity of the Zn-free Sm–Fe–N magnets decreased with increasing sintering temperature above 400 °C, while the $(BH)_{max}$ increased with increasing sintering temperature to 400 °C and thereafter decreased. The highest value of $(BH)_{max}$ was obtained upon sintering at 400 °C, and the coercivity and $(BH)_{max}$ of the Zn-free Sm–Fe–N magnet sintered at 400 °C were 0.86 MA·m^{-1} and 188 kJ·m^{-3}, respectively. In a previous paper, Soda et al.[11] reported a $(BH)_{max}$ of approximately 160 kJ·m^{-3} and a coercivity of approximately 0.57 MA·m^{-1} for a Zn-free Sm–Fe–N magnet with an oxygen content of 0.45 wt%, and our group[12] reported a $(BH)_{max}$ of 179 kJ·m^{-3} and a coercivity of 0.80 MA·m^{-1} for a Zn-free Sm–Fe–N magnet prepared via low oxygen process. The $(BH)_{max}$ value of 188 kJ·m^{-3} obtained in this study exceeds these previously reported values. As shown in Fig. 3(b), the coercivity of the Zn-bonded Sm–Fe–N magnets increased with increasing sintering temperature, and the highest H_{cJ} of 1.66 MA·m^{-1} was

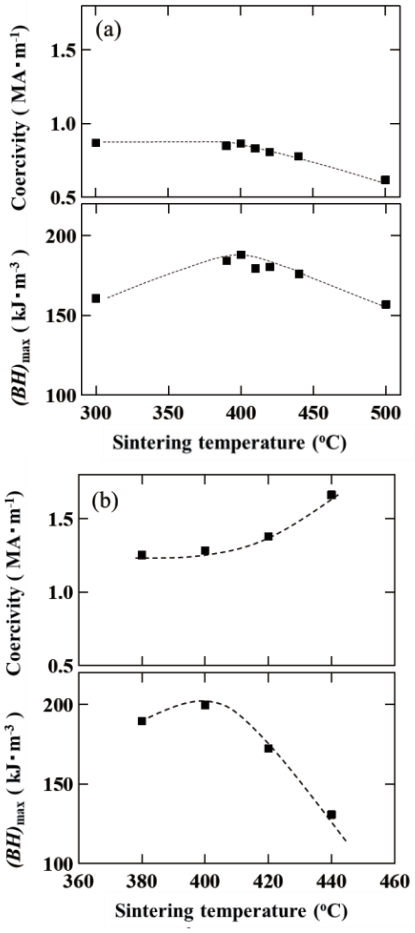

Fig. 3 Dependence of coercivity and $(BH)_{max}$ on sintering temperature for (a) Zn free and (b) Zn-bonded Sm–Fe–N magnets.

obtained upon sintering at 440 °C. In contrast, the remanence and $(BH)_{max}$ of the Zn-bonded Sm–Fe–N magnets increased with increasing sintering temperature at 400 °C, and it decreased with increasing sintering temperature above 400 °C. The highest value of $(BH)_{max}$ of 200 kJ·m^{-3} was obtained upon sintering at 400 °C, which was accompanied by a relatively high H_{cJ} of 1.28 MA·m^{-1}. Compared with the previous studies[3–7,12,16,17,20], the $(BH)_{max}$ and coercivity obtained in this study are higher. Figure 4 presents demagnetization curves for the Zn-free and Zn-bonded Sm–Fe–N magnets sintered at 400 °C. The relative densities of the Zn-free and Zn-bonded Sm–Fe–N magnets were 81% and 91%, respectively. The $(BH)_{max}$ of the Zn-bonded magnets was higher than that of the Zn-free magnets in this study owing to the higher relative density of the former. Therefore, Zn is an effective binder for increasing not only the coercivity but also the density of the magnets. The oxygen content of the Zn-bonded magnets was only 0.28 wt%, which is only a slight increase from the value measured for the mixed Sm–Fe–N/Zn powder (0.27 wt%). This oxygen content of the Zn-bonded Sm–Fe–N magnets is lowest than those reported in previous papers[11,12].

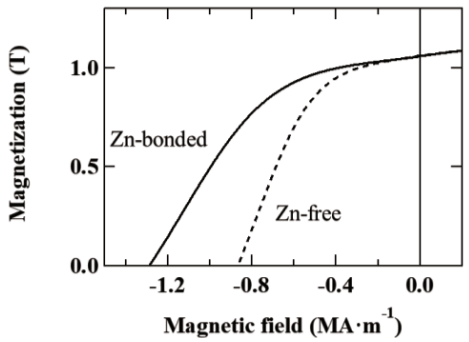

Fig. 4 Demagnetization curves for the Zn-free and Zn-bonded Sm–Fe–N magnets sintered at 400 °C.

As thermal stability is an important property for Sm–Fe–N magnets, the temperature coefficient of coercivity ($\alpha(H_{cJ})$) was evaluated for the Zn-free and Zn-bonded Sm–Fe–N magnets. Figure 5 shows the temperature dependences of coercivity for the Zn-free and Zn-bonded magnets measured using a pulsed B–H loop tracer over the temperature range from 25 to 200 °C. The open square and triangle indicate the coercivities measured at room temperature after the measurements at 200 °C, which were almost identical to the initial values. This result indicates that the influence of oxygen in the Zn-free and Zn-bonded magnets on their coercivities was negligible. The $\alpha(H_{cJ})$ values from 25 to 200 °C for the Zn-free and Zn-bonded magnets were −0.40% ·°C^{-1} and −0.34% ·°C^{-1}, respectively. In previous papers[9,14,15], the $\alpha(H_{cJ})$ values reported for Sm–Fe–N magnets without additional elements ranged from −0.45 to −0.47% ·°C^{-1}, demonstrating the superiority of the Zn-free Sm–Fe–N magnets prepared in this study. In regard to the Zn-bonded magnet, Wall et al.[16] reported an $\alpha(H_{cJ})$ value from 25 to 150 °C of −0.36% ·°C^{-1} for a 5 wt% Zn-bonded Sm–Fe–N magnet. Furthermore, Kou et al.[17] fabricated Zn-bonded magnets containing 5 and 15 wt% Zn, which displayed $\alpha(H_{cJ})$ values of approximately −0.36% ·°C^{-1} and −0.37% ·°C^{-1}, respectively (we should note that $\alpha(H_{cJ})$ values were not reported in this paper; therefore, we estimated these $\alpha(H_{cJ})$ values from the published data). In addition, our group[10] previously reported an $\alpha(H_{cJ})$ value of −0.32% ·°C^{-1} for a 15 wt% Zn-bonded Sm–Fe–N magnet. Thus, the $\alpha(H_{cJ})$ value of −0.34% ·°C^{-1} obtained for the 10 wt% Zn-bonded magnet in this study is reasonable considering its Zn content.

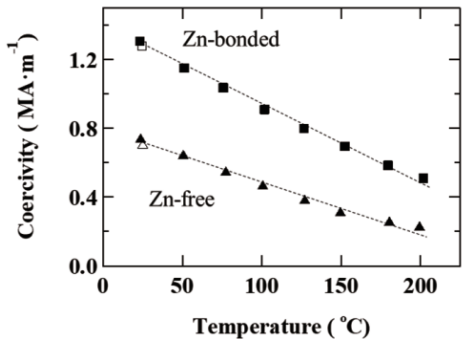

Fig. 5 Coercivities of the Zn-free and Zn-bonded Sm–Fe–N magnets measured from 25 to 200 °C. The open square and triangle indicate the coercivities measured at room temperature after the measurements at 200 °C.

The Kronmüller equation[18] is frequently applied to explain the coercivity of various samples by evaluating the values of the coefficient α and N_{eff}. Here, the Kronmüller equation is expressed as follows:

$$\mu_0 H_{cJ} = \alpha \mu_0 H_A - N_{eff} J_s \quad (1)$$

Sagawa and Hirosawa[19] applied this equation to Nd–Fe–B and Pr–Fe–B sintered magnets, and they mentioned that the first term on the right-hand side of the equation represents the nucleation field of the reversed magnetic domains, while the second term takes into account the local stray fields. They also mentioned that it is presumed that α and N_{eff} are related to the microstructure of the magnet. Thus, the α and N_{eff} values of the Zn-free and Zn-bonded Sm–Fe–N magnets prepared in this study were evaluated from the temperature dependence of H_{cJ}. Figure 6 presents a plot of $\mu_0 H_{cJ}/J_s$ against $\mu_0 H_A/J_s$ for the Zn-free and Zn-bonded Sm–Fe–N magnets. In this study, we used the temperature dependence of H_A reported in a previous paper[20]. A liner relationship was observed between the two quantities, allowing the values of α and N_{eff} to be evaluated from the gradients and intercepts of the lines of best fit. The α and N_{eff} values of the Zn-free magnet were 0.065 and 0.42, respectively, whereas those of the Zn-bonded magnet were 0.088 and 0.32, respectively. Iriyama et al.[20] reported α and N_{eff} values of 0.045 and 0.22, respectively, for a Zn-bonded Sm–Fe–N magnet containing 10 wt% Zn, and α and N_{eff} values of 0.084 and 0.23, respectively, for a Zn-bonded Sm–Fe–N magnet containing 30 wt% Zn. The α value of 0.088 obtained for the Zn-bonded magnet in this study is higher than the Zn-bonded magnet in the previous paper[20]. The N_{eff} values obtained for the magnets in this study are slightly higher than those reported in the

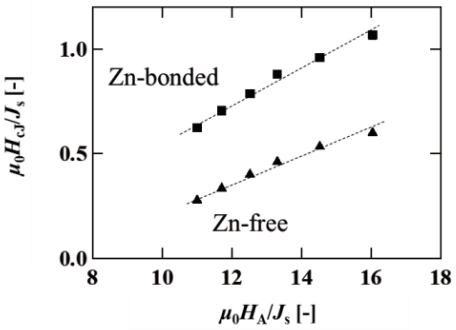

Fig. 6 Plot of $\mu_0 H_{cJ}/J_s$ versus $\mu_0 H_A/J_s$ for the Zn-free and Zn-bonded Sm–Fe–N magnets sintered at 400 °C.

previous paper[20]. These results suggested that the surface state of the $Sm_2Fe_{17}N_x$ phase may have been altered by the Zn addition. Thus, the microstructures of the Zn-free and Zn-bonded Sm−Fe−N magnets were examined via SEM and TEM. Figure 7 presents cross-sectional secondary electron and Zn-mapping images of the magnets. Zn was found to be present at the grain boundaries of the Sm−Fe−N particles in the Zn-bonded magnet. Comparison of the Zn-free and Zn-bonded magnets in Figs. 7(a) and (b) revealed a higher density for the latter sample. Next, the detailed microstructure at the grain boundary was examined via TEM. Figure 8 presents a TEM image and Sm-, Fe- and Zn-mapping images of a grain boundary in the Zn-bonded magnet. As shown in Fig. 8(d), Zn was detected at the surface of the $Sm_2Fe_{17}N_x$ phase. In contrast, as shown in Fig. 8(c), the Fe content in this region was low. Therefore, it is thought that Zn diffused along the grain boundary and reacted with the surface of the $Sm_2Fe_{17}N_x$ powder. It is suggested that this diffusion and reaction between the Zn and $Sm_2Fe_{17}N_x$ phase could be responsible for increasing the value of a and coercivity of the Zn-bonded magnet.

Consequently, in this study, Zn-free and Zn-bonded Sm−Fe−N magnets exhibiting high $(BH)_{max}$ value were successfully prepared by using Sm−Fe−N and Zn powders with low oxygen contents in conjunction with SPS.

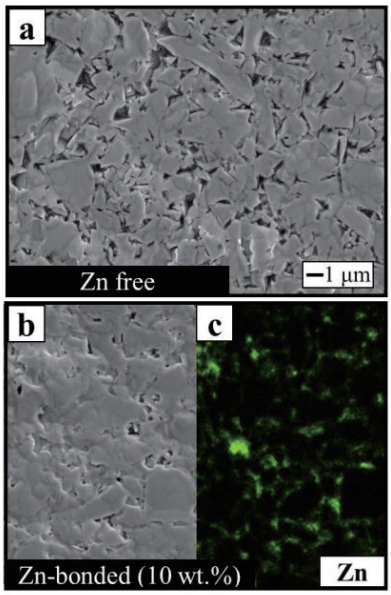

Fig. 7 SEM and Zn-mapping images of the (a)Zn-free and (b)(c)Zn-bonded Sm−Fe−N magnets.

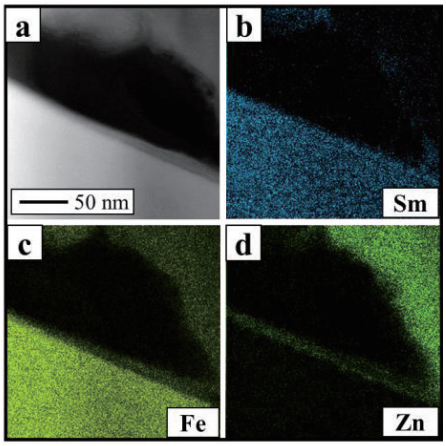

Fig. 8 (a)TEM image and (b)Sm-, (c)Fe- and (d)Zn-mapping images of a grain boundary in the Zn-bonded magnet.

4. Summary

To increase the $(BH)_{max}$ of Zn-bonded Sm−Fe−N magnets, we applied a process for preparing Sm−Fe−N and Zn powders with low oxygen contents in combination with SPS. The oxygen content, remanence, and coercivity of the Sm−Fe−N powder were 0.22 wt%, 151 A·m^2·kg^{-1}, and 0.72 MA·m^{-1}, respectively, and the oxygen content and secondary average particle size of the Zn powder were 0.083 wt% and 0.93 μm, respectively. The magnetic properties of the Zn-free Sm−Fe−N magnets included a $(BH)_{max}$ of 188 kJ·m^{-3} and an H_{cJ} of 0.86 MA·m^{-1}, and the Zn-bonded (10 wt%) Sm−Fe−N magnets exhibited excellent magnetic properties with a $(BH)_{max}$ of 200 kJ·m^{-3} and an H_{cJ} of 1.28 MA·m^{-1}. Compared with previous studies, this is the high $(BH)_{max}$ observed for a Sm−Fe−N bulk magnet simultaneously displaying a high H_{cJ}. The oxygen content of the Zn-bonded Sm−Fe−N magnets was 0.28 wt%, which was only a slight increase from the value observed for the mixed Sm−Fe−N/Zn powder (0.27 wt%). This oxygen content is the lowest reported for a Zn-bonded Sm−Fe−N magnet. Furthermore, the temperature coefficients of coercivity of the magnets were evaluated, revealing values of −0.40%·°C^{-1} and −0.34%·°C^{-1} for the Zn-free and Zn-bonded magnets, respectively. Consequently, the procedure described in this paper allows the preparation of high-performance Sm−Fe−N bulk magnets.

Acknowledgments The authors thank Sumiko Kunitomi Denshi Co. Ltd for supplying the Sm−Fe powder. We are also grateful to Dr Kobayashi, Mr. Tanno, and Ms. Yamamoto for their assistance with the TEM analysis.

This work was partially supported by Toyota Motor Corporation, the Future Pioneering Program "Development of magnetic material technology for high-efficiency motors" (MgaHEM) commissioned by the New Energy and Industrial Technology Development Organization (NEDO), and the Elements Strategy Initiative Center for Magnetic Materials (ESICMM), Grant number JPMXP 0112101004, through the Ministry of Education, Culture, Sports, Science and Technology (MEXT) of Japan.

References

1) Y. Otani, A. Moukarika, H. Sun, J.M.D. Coey, E. Devlin, and R. Harris: *J. Appl. Phys.*, **69**, 6735 (1991).
2) T. Mashimo, X. huang, S. Hirosawa, K. Makita, Y. Kato, S. Mitsudo and M. Motokawa: *J. Magn. Magn. Mater.*, **210**, 109 (2000).
3) S. Ito, M. kikuchi, T. Fujii and T. Ishikawa: *J. Magn. Magn. Mater.*, **270**, 15 (2004).
4) D. Ishihara, M. Matsuura, N. Tezuka and S. Sugimoto: Proc. 22nd Int. Workshop RE Perm. Magnets and Appl., ed. by H. Fukunaga and S. Sugimoto, Nagasaki Japan, 2012, p. 232.
5) K. Kataoka, M. Matsuura, N. Tezuka, and S. Sugimoto: *Mater. Trans.*, **56**, 1698 (2015).
6) T. Saito: *Mater. Sci. Eng. B*, **167**, 75 (2010).
7) D. Prabhu, H. Sepehri-Amin, C. L. Mendis, T. Ohkubo, K. Hono and S. Sugimoto: *Scr. Mater.*, **67**, 153 (2012).
8) K. Takagi, H. Nakayama, and K. Ozaki: *J. Magn. Magn. Mater.*, **324**, 2336 (2012).
9) N. Imaoka, T. Iriyama, S. Itoh, A. Okamoto, and T. Katsumata: *J. Alloy. Compd.*, **222**, 73 (1995).
10) M. Matsuura, T. Shiraiwa, N. Tezuka, S. Sugimoto, T. Shoji, N. Sakuma, and K. Haga: *J. Magn. Magn. Mater.*, **452**, 243 (2018).
11) R. Soda, K. Takagi, M. Jinno, W. Yamaguchi, and K. Ozaki: *AIP Adv.*, **6**, 115108 (2016).
12) M. Matsuura, Y. Nishijima, N. Tezuka, S. Sugimoto, T. Shoji, and N. Sakuma: *J. Magn. Magn. Mater.*, **467**, 64 (2018).
13) T. Ishikawa, T. Iseki, K. Yokosawa, K. Watanabe, and K. Ohmori: *IEEJ Trans FM*, **124**, 881 (2004).
14) M. Tobise, M. Shindoh, H. Okajima, K. Ishikawa, and N. Tokunaga: *IEEE Trans. Magn.*, **35**, 3259 (1999).
15) S. Yoshizawa, T. Ishikawa, I. Kaneko, S. Hayashi, A. Kawamoto, and K. Ohmori: *IEEE Trans. Magn.*, **35**, 3340 (1999).
16) B. Wall, M. Katter, W. Rodewald, and M. Velicescu: *IEEE Trans. Magn.*, **30**, 675 (1994).
17) X.C. Kou, E.H.C.P. Sinnecker, and R. Grössinger: *IEEE Trans. Magn.*, **31**, 3638 (1995).
18) H. Kronmüller: *Phys. Status Solidi (b)*, **144**, 385 (1987).
19) M. Sagawa, and S. Hirosawa: *J. Mater. Res.*, **3**, 45 (1988).
20) T. Iriyama, A. Okamoto, N. Imaoka, H. Kato, J. Shiomi, Y. Nakagawa, H. Aruga Katori, and T. Goto: *J. Magn. Soc. Jpn.*, **18**, 782 (1994).

Received Oct. 31, 2019; Accepted Jan. 30, 2020

J. Magn. Soc. Jpn., **44**, 70-74 (2020)

<Paper>

Synthesis and magnetic properties of $M^{2+}Ti^{4+}$ substituted $Ba_{12}Fe_{28}Ti_{15}O_{84}$

N. Yasuda,[1] S. Kittaka,[2] Y. Kono,[3] T. Sakakibara,[2] K. Kakizaki,[1] K. Kamishima[1]

[1]Graduate School of Science and Engineering, Saitama University, *255 Shimo-Okubo, Saitama 388-0825 Japan*

[2]Institute for Solid State Physics (ISSP), The University of Tokyo, *5-1-5 Kashiwa, Chiba 277-8581 Japan*

[3]Department of Physical Science, Osaka Prefecture University, *1-1 Gakuen-cho, Osaka 599-8531 Japan*

We investigated the synthesis conditions and magnetic properties of M-Ti substituted $Ba_{12}Fe_{28}Ti_{15}O_{84}$ with initial compositions of $Ba_{12}Fe_{28-2x}Ti_{15+x}M_xO_{84}$ (M = Zn, Mg, Ni, Cu, and Co) sintered at 1100-1300°C. The highest substitution amounts of M-Ti for Fe were consistent with the Ti-ion preference of each transition metal site reported before, suggesting that substituted Ti ions also preferred the sites with high Ti-ion occupancies. The spontaneous magnetizations and Curie temperatures were decreased as the substitution amount x was increased, which means that the substitution weakened the super-exchange interactions between Fe-O-Fe. The highest Zn-Ti substitution rate was lower than the other M-Ti substitution rates, which implies that Zn ions tend to enter specific M(2) and M(14) sites in $Ba_{12}Fe_{28}Ti_{15}O_{84}$. The sweep of the magnetic field from 0 to 80 kOe changed the relative dielectric constant of $Ba_{12}Fe_{28}Ti_{15}O_{84}$ by 0.283%. This variation of the dielectric constant caused by the application of magnetic fields is not negligible, showing that this compound should be categorized as a multiferroic material.

Key words: Ferrimagnetic iron oxides (ferrite), multiferroics, $Ba_{12}Fe_{28}Ti_{15}O_{84}$,

1. Introduction

Multiferroic materials with both magnetic and dielectric properties are attracting much interest.[1-4] They have potential applications in next-generation devices such as memory devices and sensors.

A barium-iron oxide, $BaFe_{12}O_{19}$, has high saturation magnetization and high coercivity, widely used as permanent magnets and microwave absorbers. [5), 6)] On the other hand, another barium-titanium oxide, $BaTiO_3$ (BTO), is a typical ferroelectric material, widely used as a dielectric material or a piezoelectric component. These conventional materials encouraged expectation for Ba-Fe-Ti oxides as multiferroic materials, which led to an extensive investigation of the Ba-Fe-Ti oxides system. [7)] Siegrist *et al.* showed the existence of at least 16 different compounds. [7)] Our attempts to prepare these compounds corresponding to their stoichiometry often produced multiple phases, indicating the difficulty in the synthesis. This paper focuses on one of the oxides, $Ba_{12}Fe_{28}Ti_{15}O_{84}$.

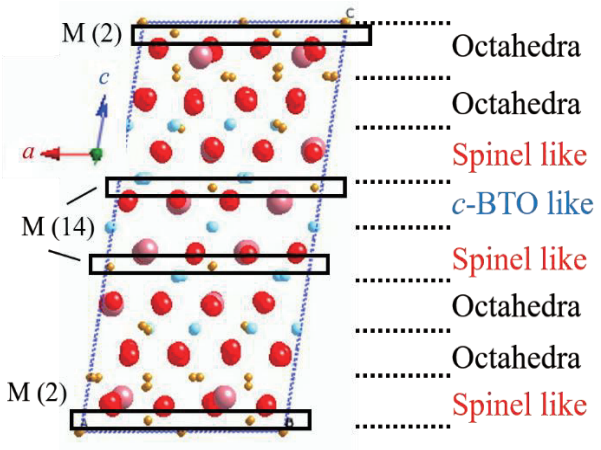

Fig. 1 Structure of $Ba_{12}Fe_{28}Ti_{15}O_{84}$. The red ions are O^{2-}, and the pink ones are Ba^{2+}. The yellow and light blue ones are transition metal cations, where the majority is Fe^{3+} for yellow and Ti^{4+} for light blue.

$Ba_{12}Fe_{28}Ti_{15}O_{84}$ has monoclinic $C2/m$ symmetry with the unit cell parameters of a = 9.988 Å, b = 17.298 Å, c = 19.17 Å, and β = 99.33°. [8)] Curecheriu *et al.* reported that this material has the saturation magnetization of 12.5 emu/g at room temperature and the Curie temperature of T_C=420 K.[9)] The crystal structure consists of spinel-like and BTO-like building blocks along the c-axis direction, as shown in Fig. 1. Tetrahedral M(2) and M(14) sites are emphasized for discussion later. The indispensable role that spinel blocks play in the magnetism of $BaFe_{12}O_{19}$, combined with the ferroelectric BTO structure blocks, has led to the expectation for multiferroic properties for $Ba_{12}Fe_{28}Ti_{15}O_{84}$. In addition, the magnetic properties of the M-type hexaferrite can also be changed by the substitution of M^{2+} and Ti^{4+} cations for $2Fe^{3+}$ cations where M^{2+} is a divalent transition-metal cation.[10-14)] However, there is a limited number of publications about other hexaferrites with this substitution, possibly due to the less stability of non-M-type hexaferrites. [15), 16)] Although $Ba_{12}Fe_{28}Ti_{15}O_{84}$ has a structural similarity with these hexaferrites that the stacking of spinel and other blocks forms, no previous study has investigated the substitution effect on $Ba_{12}Fe_{28}Ti_{15}O_{84}$. The specific objective of this study was to synthesize M^{2+}-Ti^{4+} substituted $Ba_{12}Fe_{28}Ti_{15}O_{84}$ samples for controlling multiferroic characteristics because this substitution increases the titanium content in the BTO-like blocks in the structure of $Ba_{12}Fe_{28}Ti_{15}O_{84}$.

2. Experimental procedure

Samples were prepared by a conventional ceramic method. We used $BaCO_3$, α-Fe_2O_3, TiO_2, ZnO, MgO, NiO, CuO, and CoO as starting materials. They were mixed in

a desired proportion, $Ba_{12}Fe_{28-2x}Ti_{15+x}M_xO_{84}$ (M = Zn, Mg, Ni, Cu, or Co) in a planetary micro mill (Fritsch, PULVERISETTE 7) for 10 minutes at the rate of 1100 r.p.m. The mixed powders were pressed into disks and then sintered at 1100-1300˚C in air for 5 h. Finally, the products were ground into powders in a mortar.

The crystal structures were examined by powder X-ray diffraction (XRD) with Cu-Kα radiation. The magnetizations were measured with a vibrating sample magnetometer (Tamakawa, TM-VSM2130HGC), and a superconducting quantum interference device (SQUID) magnetometer (Quantum Design, MPMS-XL). The relative dielectric constant was calculated from capacitance. The capacitance was measured by a three-terminal capacitance method with a capacitance bridge (ANDEEN-HAGERLING, AH 2500A).

3. Results and discussion

Figure 2 shows the X-ray diffraction patterns of $Ba_{12}Fe_{28-2x}Ti_{15+x}M_xO_{84}$ at highest substitution x_{max} for each element. Most of the samples were sintered at 1300 ˚C except for the highest Cu-Ti substituted sample sintered at 1100˚C. These samples exhibited single phase of $Ba_{12}Fe_{28}Ti_{15}O_{84}$, demonstrating the success in the M-Ti substitution. The lattice constants of each sample showed slight changes within 0.1 %, even at the maximum substitution.

These maximum substitution values of x_{max} are found to be lower than 4, which suggests possible preference of Ti ions for specific sites in the unit cell. Arranging the transition metal sites in the order of Ti-ion occupancies, we can find that there is a large difference between the fifth-highest M(15) site and the sixth-highest M(11) site. Assuming that the substituted Ti ions occupy the sites from the first to the fifth, the substitution amount can be estimated to be $x = 4.0$. The values of x_{max} of Co-Ti, Mg-Ti, Ni-Ti, and Cu-Ti substituted samples are consistent with this estimation.

Figure 3 shows spontaneous magnetization of $Ba_{12}Fe_{28-2x}Ti_{15+x}M_xO_{84}$ at T=5 K as a function of M-Ti substitution amount x. The spontaneous magnetization was estimated by linear extrapolation of each magnetization curves from a high field region. Although both Zn and Mg are nonmagnetic ions, Zn-Ti substitution decreased the spontaneous magnetization steeper than Mg-Ti substitution. Since Zn ions are generally apt to prefer tetrahedral sites,[17), 18)] Zn ions likely sit at just two sites (M(2) and M(14) shown in Fig. 1) in the unit cell of $Ba_{12}Fe_{28}Ti_{15}O_{84}$, which possibly leads to the lower substitution limit than those of the other M-Ti substituted samples. Therefore, it is reasonable to assume that Fe ions at these tetrahedral sites align in

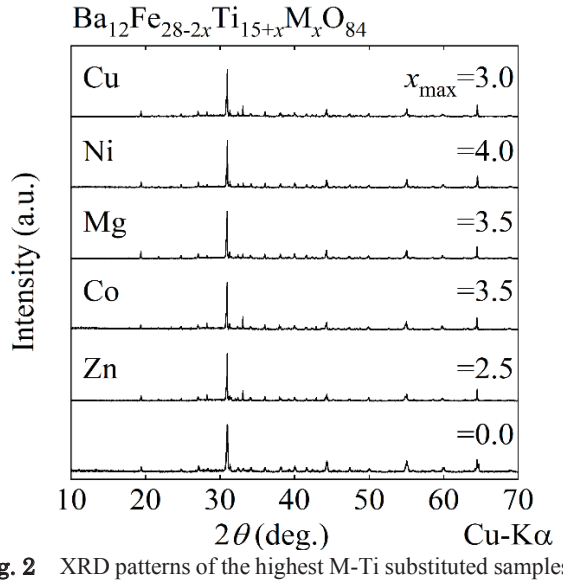

Fig. 2 XRD patterns of the highest M-Ti substituted samples of $Ba_{12}Fe_{28-2x}Ti_{15+x}M_xO_{84}$

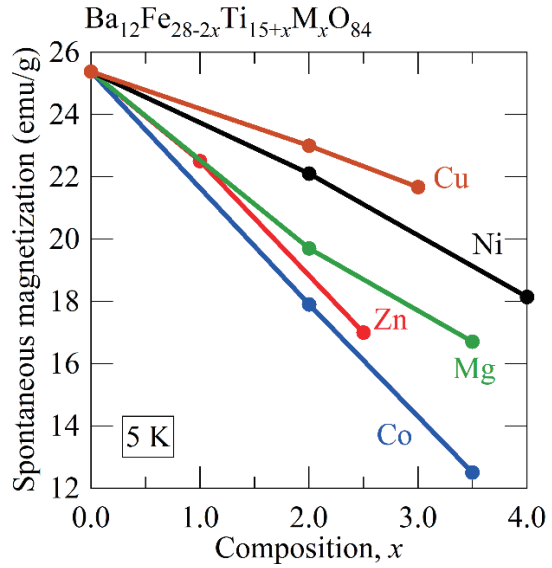

Fig. 3 M-Ti substitution dependence of spontaneous magnetization of $Ba_{12}Fe_{28}Ti_{15}O_{84}$

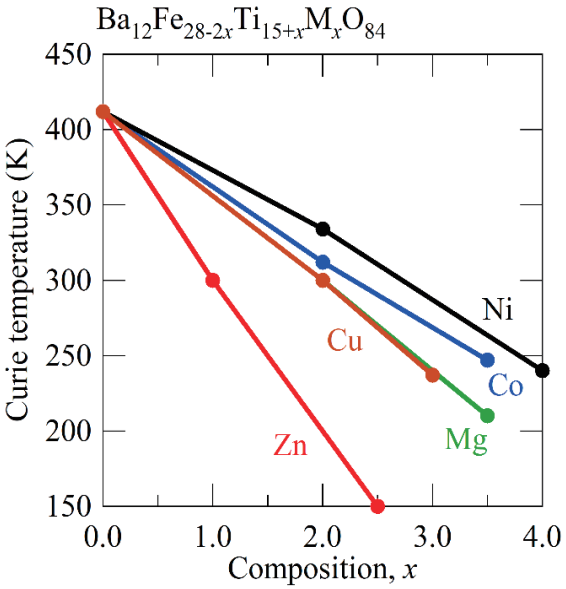

Fig. 4 M-Ti substitution dependence of Curie temperature of $Ba_{12}Fe_{28}Ti_{15}O_{84}$

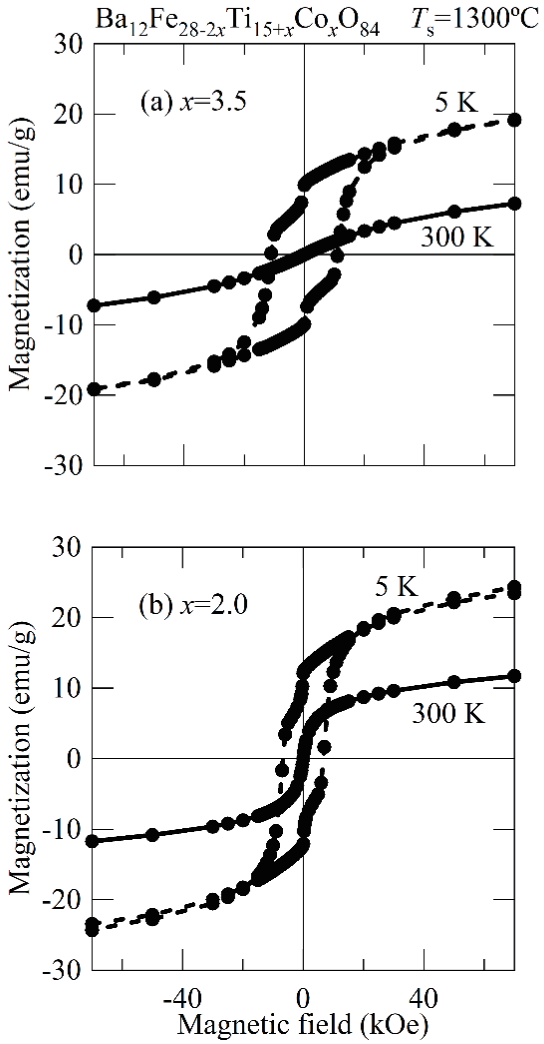

Fig. 5 *M-H* loops of Co-Ti substituted samples at (a) x=3.5 and (b) x=2.0

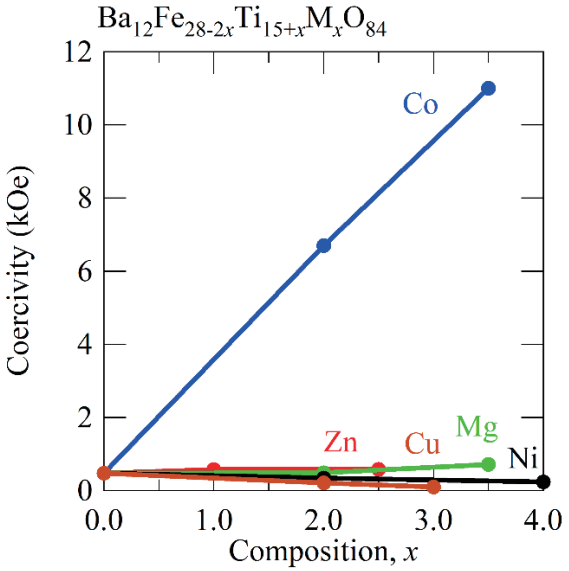

Fig. 6 M-Ti substitution dependence of coercivity of $Ba_{12}Fe_{28}Ti_{15}O_{84}$

the up-spin direction. The spontaneous magnetizations of Co-Ti substituted samples were smaller than those of the other substituted samples because of the relatively higher magnetic susceptibilities of the Co-Ti substituted samples at high magnetic fields from which the spontaneous magnetizations were derived by extrapolation.

Figure 4 shows Curie temperature of $Ba_{12}Fe_{28-2x}Ti_{15+x}M_xO_{84}$ as a function of x. These linear decreases in the spontaneous magnetization and the Curie temperature with increasing x imply that M and Ti cations were successfully substituted for Fe cations in $Ba_{12}Fe_{28}Ti_{15}O_{84}$, which weakened the super-exchange interactions between Fe-O-Fe. The Curie temperature of Zn-Ti substituted samples more sharply decreased than those of other M-Ti substituted samples with increasing x. This result suggests that Zn ions tend to enter the sites of significant importance in magnetic interactions between Fe-O-Fe.

Figure 5 shows the *M-H* loops of the Co-Ti substituted samples at (a) x=3.5 and (b) x=2.0 measured at T=5 K. Former sample at x=3.5 exhibited a large coercivity of 11 kOe and latter sample at x=2.0 also showed a large coercivity of 6.7 kOe. These results mean that the higher substitution of Co resulted in the higher coercivity, possibly due to the anisotropy of Co cations in contrast with the soft magnetic properties accompanying the other divalent-cation-substituted samples as shown in Fig. 6. Furthermore, these Co-Ti substituted samples had two different slopes in their magnetization curves. The temperature dependence of magnetization of each sample clearly showed just one Curie temperature, as shown in Fig. 7, demonstrating the existence of a single magnetic phase. Therefore, it is reasonable to assume the coexistence of two kinds of spin components that respond to magnetic field differently even in the same crystal

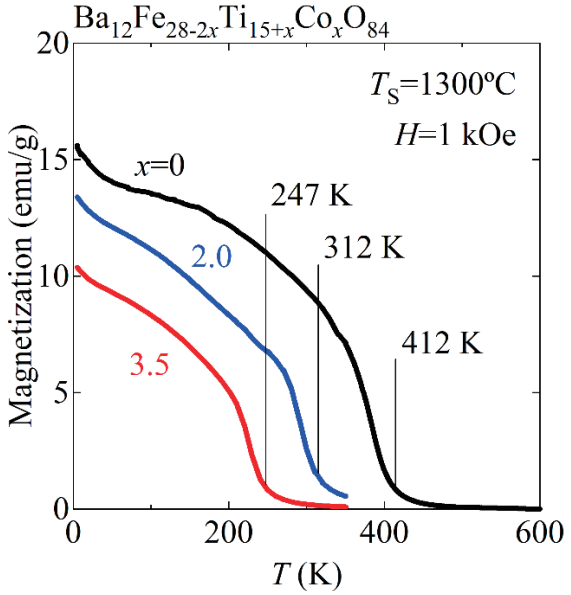

Fig.7 Temperature dependences of magnetization of Co-Ti substituted samples at x=3.5, x=2.0, and x=0.

lattice. These coercivities were not observed at 300 K. It seems likely that the rise in temperature weakened the anisotropy one of the two spin components possessed and decreased the coercivity, which is consistent with the absence of anomaly in the temperature dependence of magnetization except for the Curie temperature.

Figure 8 shows the field dependence of the relative dielectric constant of $Ba_{12}Fe_{28}Ti_{15}O_{84}$ at T=1.6 K. We first applied a magnetic field up to 80 kOe, decreased it to -20 kOe, and swept it back to zero. The relative dielectric constant was calculated by the formula $C=\varepsilon_0\varepsilon_r S/d$ (C : capacitance, ε_0 : vacuum permittivity, ε_r : relative permittivity, S : the area of the sample, d : the thickness of the sample). The change in permittivity was about 0.283% between H=0 kOe and 80 kOe. This change in the dielectric constant may come from magnetostriction that depends on magnetization processes. However, the magnetization process in Fig. 9 shows a less steep increase above 20 kOe than that at low magnetic fields in spite that the dielectric constant was still significantly changed above 20 kOe as shown in Fig. 8. This variation of the dielectric constant cannot be simply explained by magnetostriction. Therefore, this compound is a possible candidate as a multiferroic material because a magnetic field can control the dielectric constant. The other sintered bulk samples with M-Ti substitutions were brittle or fragile, which prevented us from measuring their dielectric properties in magnetic fields except for the starting material of $Ba_{12}Fe_{28}Ti_{15}O_{84}$. Further synthesis research should be carried out to measure the dielectric properties of other substituted samples.

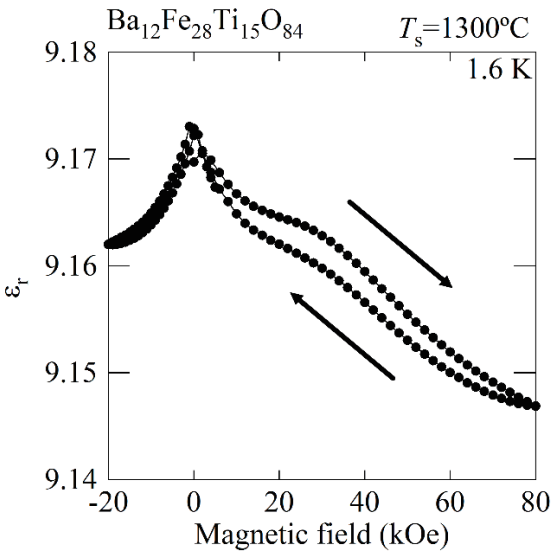

Fig. 8 Field dependence of relative dielectric constant of $Ba_{12}Fe_{28}Ti_{15}O_{84}$

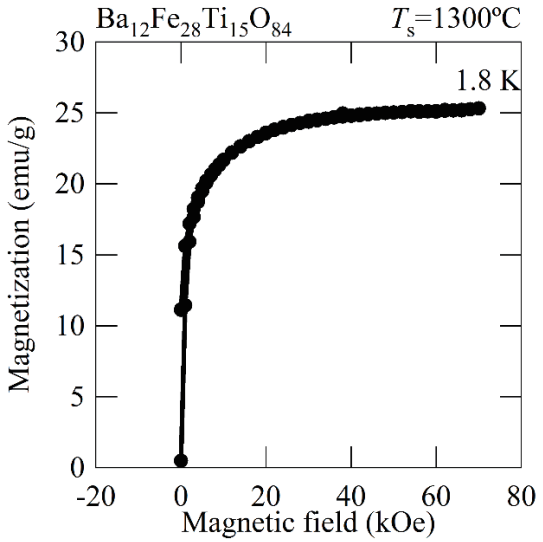

Fig. 9 *M-H* curve of $Ba_{12}Fe_{28}Ti_{15}O_{84}$

We measured the field dependence of relative permittivity of $Ba_{12}Fe_{28}Ti_{15}O_{84}$. Applying a magnetic field from 0 kOe to 80 kOe decreased the relative permittivity by 0.283%. Thus, this compound is a possible candidate as a multiferroic material because of the ability to change the dielectric property by application of a magnetic field.

4. Conclusion

We successfully synthesized M-Ti substituted samples of $Ba_{12}Fe_{28-2x}Ti_{15+x}M_xO_{84}$ (M = Zn, Mg, Ni, Cu, or Co) by a conventional ceramic method. The highest substitution amounts of x_{max} were 2.5 (Zn-Ti), 3.5 (Mg-Ti), 4.0 (Ni-Ti), 3.0 (Cu-Ti), and 3.5 (Co-Ti).

The spontaneous magnetizations and Curie temperatures were decreased as x increased. It indicates that this substitution weakened the super-exchange interactions between Fe-O-Fe.

The highest substitution amounts of M-Ti for Fe were consistent with the Ti-ion preference of each transition metal site reported before, suggesting that substituted Ti ions also preferred the sites with high Ti-ion occupancies.

Zn ions possibly sit at just two sites (M(2) and M(14)) in the unit cell of $Ba_{12}Fe_{28}Ti_{15}O_{84}$, which can lead to the lower substitution limit than those of other M-Ti substituted samples. It is possible that Fe ions at these tetrahedral sites align in the up-spin direction.

The Co-Ti substituted samples showed large coercivities at 5 K. The magnetization curves implied the coexistence of two kinds of spin components that responded to applied magnetic field differently, even in the same crystal lattice.

References

1) R. C. Pullar: *Prog. Mater. Sci.*, **57**, 1191 (2012).
2) W. Eerenstein, N. D. Mathur, and J. F. Scott: *Nature*, **442**, 759 (2006).
3) K. Taniguchi, N. Abe, S. Ohtani, H. Umetsu, and T. Arima: *Appl. Phys. Express*, **1**, 031301 (2008).
4) N. A. Hill: Annu. *Rev. Mater. Res.*, **32,** 1 (2002).
5) J. Smit and H. P. J. Wijn: Ferrites, (Philips Technical Library, Netherlands 1959).
6) S. Chikazumi: Physics of Ferromagnetism, (Oxford University Press, Oxford, 2009).

7) T. Siegrist and T. A. Vanderah: *Eur. J. Inorg. Chem.,* **2003(8)**, 1483 (2003).
8) I. E. Grey, A. Collomb, and X. Obradors: *J. Solid State Chem.,* **91,** 131 (1991).
9) L. P. Curecheriu, M. T. Buscaglia, A. C. Ianculescu, R. C. Frunza, I. V. Ciuchi, A. Neagu, G. Apachitei, A. Bassano, G. Canu, P. Postolache, L. Mitoseriu, and V. Buscaglia: *J. Phys. D: Appl. Phys.,* **44**, 435002 (2011).
10) Y. Guen, Y. Lin, L. Zou, Q. Miao, M. Zeng, Z. Liu, X. Gao, and J. Liu: *AIP Advances*, **3**, 122115 (2013).
11) Z. Yang, C. S. Wang, X. H. Li, and H. X. Zeng: *Mater. Sci. Eng.*, **B90**, 142 (2002).
12) P. Wartewig, M. K. Krause, P. Esquinazi, S. Rösler, and R. Sonntag: *J. Magn. Magn. Mater.,* **192**, 83 (1999).
13) T. Toyoda, K. Kitagawa, K. Yamawaki, T. Hanashima, S. Sasaki, and P. D. Siddons, *J. Ceram. Soc. Jpn.,* **112**, S1455 (2004).
14) J. Li, H. Zhang, Y. Liu, Q. Li, G. Ma, and H. Yang: *J. Mater. Electron*, **26**, 1060 (2015).
15) K. Watanabe, K. Kakizaki, and K. Kamishima: *J. Magn. Soc. Jpn.*, **41**, 127 (2017).
16) K. Watanabe, T. Fujihara, K. Watanabe, K. Kakizaki, and K. Kamishima: *J. Phys. Soc.* Jpn., **89**, 014704 (2020).
17) Z. W. Li, C. K. Ong, Z. Yand, F. L. Wei, X. Z. Zhou, J. H. Zhao, and A. H. Morrish: *Phys. Rev. B*, **62**, 6530 (2000).
18) K. Tanwar, D. S. Gyan, P. Gupta, S. Pandey, O. Parkash, and D. Kumar: *RSC Adv.*, **8**, 19600 (2018).

Received Feb. 06, 2020; Revised Mar. 16, 2020; Accepted Mar. 18, 2020

J. Magn. Soc. Jpn., **44**, 75-78 (2020)

<Paper>

Synthesis of $L1_2$-FeNi nanoparticles by nitrogen insertion and topotactic extraction method

S. Goto, H. Kura, and H. Yanagihara*

Advanced Research and Innovation Center, DENSO Corporation, Aichi, 470–0111, Japan

**Department of Applied Physics, University of Tsukuba, Ibaraki, 305–8573, Japan*

The nitrogen insertion and topotactic extraction (NITE) method was used to explore an unknown metastable phase of an FeNi alloy with an Fe:Ni ratio of 1:1. We found that partly ordered non-equilibrium $L1_2$-FeNi can be obtained through Fe_2Ni_2N as the intermediate nitride phase. The experimental results of both x-ray diffraction and transmission electron microscopy with energy dispersive x-ray spectrometry are consistent in identifying the denitrided material as $L1_2$-FeNi. Ni atoms preferentially occupy the corner sites in an estimated 96% of cases. No significant difference was found in the magnetization curves between the precursor of $A1$-FeNi and $L1_2$-FeNi particles. Our results suggest that the NITE method is not only a useful way for synthesizing fully ordered alloys of equilibrium phases such as $L1_0$-FeNi but also for creating metastable phases like $L1_2$-FeNi.

Key words: soft magnetic material, super lattice structure, nanoparticle

1. Introduction

An ordered alloy of $L1_0$-FeNi[1)-3)] with a structural transition temperature as low as 594 K [4)-6)] was recently synthesized using the nitrogen insertion and topotactic extraction (NITE) method.[7)] The NITE method consists of two steps; 1) nitriding particles of a disordered alloy to synthesize an ordered nitride compound; and then 2) topotactically removing the nitrogen[8)9)] while maintaining the relative atomic positions of the other elements. Using this process, high purity $L1_0$-FeNi particles are obtained if the intermediate nitride is FeNiN.[7)] The FeNiN has a tetragonal crystal structure, in which Fe and Ni are regularly arranged in layers. FeNiN is an anti-ferromagnetic material with a Néel temperature (T_N) of 177 K.[10)] In this structure, the FeN layers and the Ni layers are alternately stacked along the [001] direction, which is likely due to the higher affinity for Fe-N than for Ni-N.[11)] Meanwhile, the only difference in the atomic positioning of FeNiN and that of $L1_0$-FeNi is that in one, the N atoms are located between Fe atoms on Fe layers or not. Therefore, $L1_0$-FeNi is produced by reducing the number of nitrogen atoms in FeNiN. Thus, the NITE method has the potential to synthesize various ordered alloys through the nitride phases. Unlike conventional metallurgical methods, the NITE technique involves the use of chemical processes in alloy synthesis. Metallic compounds synthesized by the NITE method could have many potential applications besides $L1_0$-FeNi.

There are several different phases reported for an Fe-Ni-N system. Fe_2Ni_2N[8)12)-14)] is an FeNi nitride system with a lower degree of nitridation than FeNiN. For example, Fe_2Ni_2N has a perovskite structure as shown in Fig. 1 (a). In this system, the corner sites are fully occupied by Ni atoms and the face center sites are occupied by Fe and Ni atoms with a ratio of 2:1. Moreover,

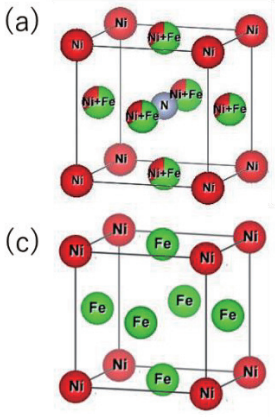

Fig. 1 Crystal structure models of (a)Fe_2Ni_2N, (b)$L1_2$-FeNi, and (c) $L1_2$-Fe_3Ni. VESTA was used for drawing the crystal structures.

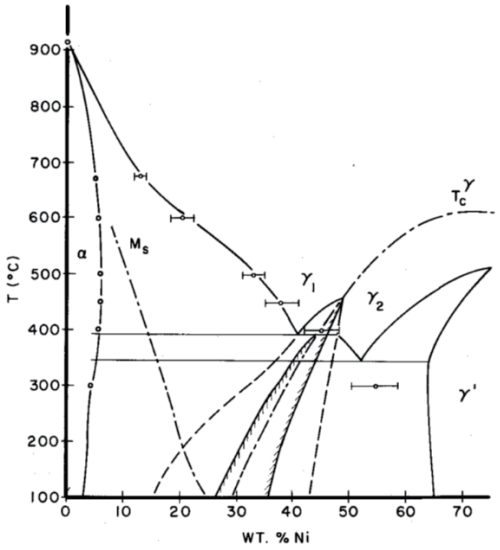

Fig. 2 Fe-Ni phase diagram calculated by K.B. Reuter et al.[15)]

the body center position is occupied by N atoms. Therefore, it would be possible to obtain an ordered alloy by performing a denitriding treatment on Fe_2Ni_2N if both the Ni and Fe atoms remain at their original positions. The expected crystal structure of the FeNi ordered alloy obtained by the denitriding treatment of Fe_2Ni_2N is shown in Fig. 1(b) and can be expressed as the $L1_2$-phase of FeNi alloy. As shown in Fig. 2, such an ordered phase is not found in the phase diagram of the Fe - Ni system as reported by Ying - Yu Chang et al.[15)-17)]This structure is similar to that of Fe_3Ni except for the composition ratio of Fe to Ni.

In this study, we demonstrate the process of synthesizing ordered alloys of FeNi other than $L1_0$-FeNi by the NITE method. A nitride of Fe_2Ni_2N particles are transformed into $L1_2$-FeNi alloys through the NITE process.

2. Experiment

The preparation process of Fe_2Ni_2N is described as follows. FeNi nanoparticles with two different mean diameters of 30 nm and 60 nm supplied by Nisshin Engineering as a starting material, were synthesized by the thermal plasma method. In the nitriding process starting from the particles with a 60 nm mean diameter, a single phase of Fe_2Ni_2N was obtained, whereas the experiments using 30 nm particles sometimes produced FeNiN as a second phase. Therefore, subsequent experiments were performed using particles with a diameter of 60 nm. The composition ratio of Fe and Ni in the raw material determined by X-ray fluorescence spectrometers (XRF) was $Fe_{49.7}Ni_{50.3}$. Fe_2Ni_2N was then obtained from an FeNi alloy in the form of nanoparticles in an ammonia flow.[8)] The nitriding treatment was performed in an electric furnace capable of heat treatment in an ammonia atmosphere. Approximately 1 g of FeNi nanoparticles are placed in a furnace on a quartz boat. The heat treatment was performed at 300 °C for 10 h while ammonia gas was flowing at 1 L/min. Next, heat treatment was performed at 300 °C for 1 h while hydrogen gas was flowing at 1 L/min, which is the denitriding process. The purity of both ammonia and hydrogen gases used for the nitriding and denitriding processes, respectively, was greater than or equal to 99.999%. These preparation process were optimized for the single phase formation of $L1_2$-FeNi nanoparticles. For crystal structure analysis, an X-ray diffractometer (XRD) by Rigaku was used. Fe-K_β (λ = 1.75653 Å) was used as an X-ray source in order to simplify the distinction between Fe and Ni. The atomic mapping of the crystal structure was performed with a transmission electron microscope with energy dispersive x-ray spectrometry (TEM-EDX). In order to investigate the magnetic properties, the magnetic field magnetization measurement was performed at room temperature with a vibrating sample type magnetometer (VSM).

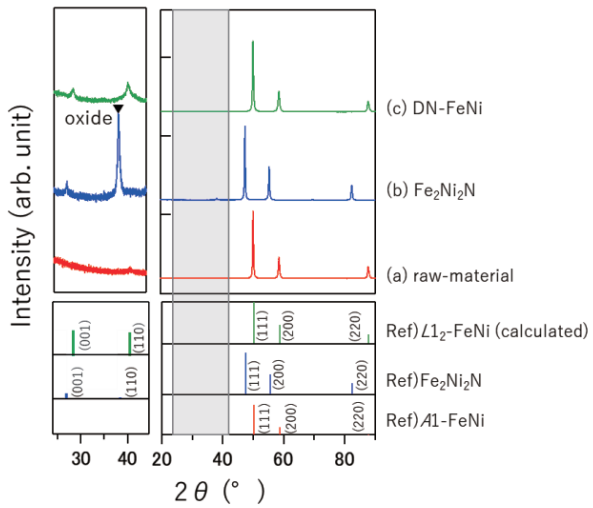

Fig. 3 XRD patterns of (a) raw material, (b) nitrided, (c) denitrided sample.

3. Results

The XRD measurement results for the particles before and after the NITE treatment are shown in Fig. 3. Experimentally obtained XRD patterns are shown in the top portion and reference patterns are shown below. The crystal structure used to calculate the XRD pattern for Fe_2Ni_2N was reported by Arnot et al.[8)] For $A1$-FeNi, we referred to the Inorganic Crystal Structure Database Collection Code (ICSD) #103556. Since the crystal structure of $L1_2$-FeNi has not been reported, we obtained both the Bragg positions and the intensities by assuming an ordered fcc structure with the lattice parameter of a = 0.358 nm, which is the same as that of the $A1$ alloy. The inset on the left side of Fig. 3 is an enlargement of the plot corresponding to the angles between 2θ = 24 and 44°. As shown in Figs. 3 (a) and (b), the position and intensity of the diffraction lines of the FeNi alloy are changed by the nitriding treatment. The diffraction peak observed at around 38° can be assigned to $NiFe_2O_4$(311). The oxide phase could be caused by the surface oxidation reactions that occur when taking the alloy out of the furnace. Since the obtained diffraction lines coincide very well with the Fe_2Ni_2N shown in the reference,[8)] we can conclude that a single phase of Fe_2Ni_2N was synthesized by the nitriding process. The observed lattice parameters for the (Fe,Ni)-N alloy suggests that the composition ratio of (Fe,Ni):N = 4:1 when taking Vegard's law into account. In order to estimate the site occupation elements in Fe_2Ni_2N, we compared the diffraction intensities $I(h\ k\ l)$ for the $(h\ k\ l)$ = (0 0 1) and $(h\ k\ l)$ = (1 1 1)peaks. The following formula was used for the calculation.

$$I(h\ k\ l) \propto L_p(\theta) \cdot |F_{hkl}|^2 \qquad (1)$$

$$F_{hkl} = \sum_{n=1}^{N} f_n \exp(2\pi i(hx_n + ky_n + lz_n)) \qquad (2)$$

$$f = f_0 + f' + if''. \qquad (3)$$

The parameters shown here are θ : Bragg angle, L_p : Lorentz polarization factor, F : crystal structure factor, f_n : atomic scattering factor of the nth atom in the unit cell, (x_n, y_n, z_n) : the coordinates of the nth atom, (h, k, l) : XRD indices, f_0 : Atomic scattering factor neglecting the binding force of electrons in the atom, f', f'' : anomalous scattering factor.

The calculated result for the ordered Fe_2Ni_2N is $I(001)/I(111) = 0.0367$. While the experimentally obtained ratio is $I(001)/I(111) = 0.036$. These results are very close to those of the ideal Fe_2Ni_2N structure in which the corner sites are preferentially occupied by Ni atoms.

Subsequently, the XRD result of the denitriding sample is shown in Fig. 3 (c). The Bragg peaks appear at the same positions as those of $A1$-FeNi, which is the starting material, indicating that the denitriding treatment completely removes nitrogen atoms from Fe_2Ni_2N and reproduces an FeNi alloy. Although surface oxidation treatment was performed after the denitriding process, no oxide peak was observed. This is thought to be because the oxide was reduced by the heat treatment in hydrogen, and the volume ratio of the oxide film was reduced because the surface area of the film was reduced due to the particle sintering. Hereafter we refer to the denitriding treatment as DN. We note that in the diffraction lines of DN - FeNi, additional peaks can be seen around $2\theta = 28.3^\circ$ and $2\theta = 40.4^\circ$, which are not seen in those locations for the disordered FeNi. In the case of the DN process used to produce $L1_0$-FeNi, both Fe and Ni atoms remain during the DN process. If a similar process occurs on our Fe_2Ni_2N particles during DN, we can expect that the DN - FeNi is not a simple disordered fcc ($A1$) structure, but an ordered fcc structure with the sites preferentially occupied by Fe or Ni.

In order to evaluate the site distributions of Ni/Fe at the corner/face-centered positions of DN-FeNi, the relationship between the Ni occupation ratio at the corner site and the intensity of XRD was calculated. Here, RIETAN - 2000 was used for the calculation of the intensity ratio. Furthermore, the Sasaki table lists the anomalous scattering factor associated with the atomic scattering factors for each nuclide and wavelength. The values obtained from the Sasaki table[18] were $f' = -4.6259$ and $f'' = 0.4742$ for $\lambda = 1.75653$ Å. The results of the calculation are shown in Fig. 4. The vertical axis shows a diffraction intensity ratio between (001) and (111), and the horizontal axis corresponds to the Ni occupation ratio at the corner position. From the results in Fig. 3(c), $I(001)/I(111)$ was found to be 0.47. This value indicates that the Ni occupation at the corner position was estimated to be 96%. This result shows that the position of the metal in the crystal structure is not notably changed before and after the denitriding treatment. From the XRD analysis results, we can conclude that DN - FeNi is $L1_2$-FeNi.

The atomic mapping using TEM-EDS for DN - FeNi is shown in Fig. 5. This image was observed from the (001) direction. Both Fe and Ni show a preferential distribution. The distribution of Fe seems to be

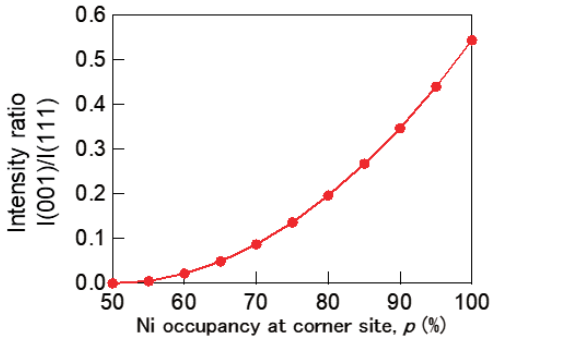

Fig. 4 Simulation of the relationship between Ni occupancy at the corner site and the intensity ratio of (001) and (111).

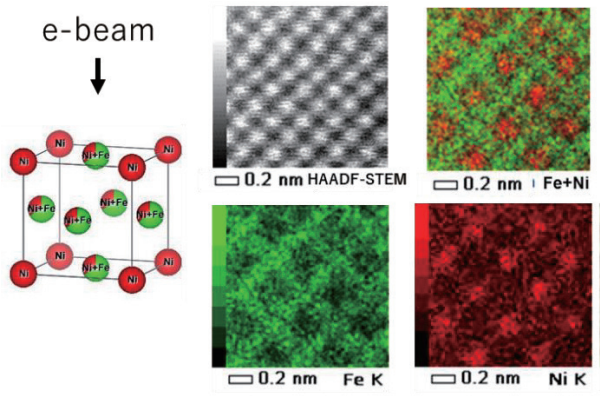

Fig. 5 TEM observation of DN-FeNi. The images show (a) HAADF image and element mapping images of (b)Fe, (c) Ni, and (d) Fe and Ni overlay.

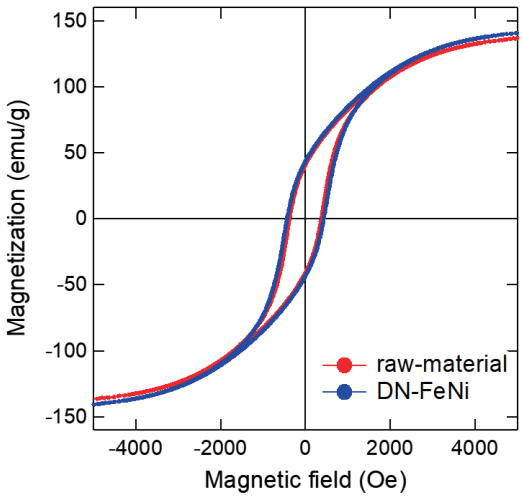

Fig. 6 Hysteresis curves of the raw material of FeNi alloy and DN-FeNi alloy.

checkerboard-like, while that of Ni seems to be a square lattice. The observed distributions are consistent with the crystal structure of the $L1_2$ type[19], where the corner site is occupied by only Ni and the face's center site is occupied by either Fe or Ni.

In order to evaluate the magnetic properties of the obtained DN - FeNi, magnetic measurements using a VSM were carried out at room temperature. The results are shown in Fig. 6. Almost no change in coercivity was observed between the raw-material and DN-FeNi. Unlike tetragonal $L1_0$-FeNi, both $A1$ - FeNi and DN - FeNi have a cubic crystal structure, so large magnetic anisotropy cannot be expected. For this reason, we believe that there was no significant change in coercivity with or without ordering. Note that the magnetization of DN-FeNi is slightly higher than that of the raw material. The magnetizations of DN-FeNi and the raw material at 5 kOe were 140 emu/g and 129 emu/g. It is considered that the composition ratio of Fe and Ni does not change during the NITE process. Therefore, this difference in magnetization is considered to be a difference in the surface oxidation state. In addition, there was no change in the magnetization process at room temperature; however there may be differences at Curie temperatures, because one is an ordered alloy and the other is a random alloy.

4. Summary

From the XRD and TEM-EDS measurements, we confirmed that the $L1_2$-FeNi alloy was synthesized as shown in Fig. 1 (b). The FeNi composition ratio is 1:1, and the analysis of the XRD diffraction intensity ratio shows that the corner site is occupied by only Ni atoms. Therefore, the face center position is randomly occupied by Fe or Ni with a 2:1 distribution. This arrangement of the Fe and Ni is the same as that in the distribution of atoms in the Fe_2Ni_2N, indicating that the topotactic denitriding treatment works in the same fashion for Fe_2Ni_2N as it does for FeNiN. Comparing the magnetization curves of $A1$ - FeNi and $L1_2$-FeNi, there were no significant differences in either the saturation magnetizations or coercive forces. We note that the $L1_2$-FeNi phase reported here has not been reported elsewhere so far. The NITE method can be expected to be used widely as a new synthesis method for ordered alloys.

Acknowledgements This paper is based on results obtained from the Future Pioneering Program "Development of magnetic material technology for high-efficiency motors" commissioned by the New Energy and Industrial Technology Development Organization (NEDO).

References

1) J.F. Petersen, M. Aydin, J.M. Knudsen: *Phys. Lett. A.,* **62**, 192 (1977).
2) M. Kotsugi, C. Mitsumata, H. Maruyama, T. Wakita, T. Taniuchi, K. Ono, M. Suzuki, N. Kawamura, N. Ishimatsu, M. Oshima, O. Watanabe, M. Taniguchi: *Appl. Phys. Express.,* **3,** 0103001 (2010).
3) J. Paulevé, A. Chamberod, K. Krebs, A. Bourret: *J. Appl. Phys.,* **39,** 989 (1968).
4) T. Mohri: *J. Mater. Sci.,* **50,** (2015).
5) J.F. Albertsen, J.M. Knudsen, N.O. Roy-Poulsen, L. Vistisen: *Phys. Scr.,* **22,** 171 (1980).
6) M. Uehara, J. Gattacceca, H. Leroux, D. Jacob, C.J. Van Der Beek: *Sci. Lett.,* **306,** 241 (2011).
7) S. Goto, H. Kura, E. Watanabe, Y. Hayashi, H. Yanagihara, Y. Shimada, M. Mizuguchi, K. Takanashi, E. Kita: *Sci. Rep.,* **7**, 1 (2017).
8) R.J. Arnott, A. Wold: *J. Phys. Chem. Solids.,* **15**, 152 (1960).
9) J.B. Goodenough, A. Wold, R.J. Arnott: *J. Appl. Phys.,* **31**, 342S (1960).
10) S. Goto, H. Kura, H. Yanagihara, E. Kita, M. Tsujikawa, R. Sasaki, M. Shirai, Y. Kobayashi, T. Honda, K. Ono, *Appl. Nano Mater.,* **11**, 6909 (2019).
11) M. Tsujikawa and M. Shirai: private communication.
12) X.G. Diao, R.B. Scorzelli, RechenbergH.R: *J. Magn. Magn. Mater.,* **218**, 81 (2000).
13) X.G. Diao, A.Y. Takeuchi, F. Garcia, R.B. Scorzelli: *J. Appl. Phys.,* **85**, 4485 (1999).
14) S.K. Chen, S. Jin, G.W. Kammlott, T.H. Tiefel., D.W. Johnson, E.M. Gyorgy: *J. Magn. Magn. Mater.,* **110**, 65 (1992).
15) K.B. Reuter, D.B. Williams, J.I. Goldstein: *Metall. Trans. A.,* **20**, 719 (1989).
16) Y.G.Y. Chuang, Y.A. Chang, R. Schmid, J.C. Lin: *Metall. Trans. A.,* **17**, 1361 (1986).
17) J.K. Van deen, F. Van Der Woude: *Acta Metall.,* **29**, 1255 (1981).
18) http://www.tsurumi.yokohama-cu.ac.jp/xtal/Sasaki-table/fpk.tbl(As of October 2, 2019).
19) M.D. Rossell, R. Erni, M. Asta, V. Radmilovic, U. Dahmen: *Phys. Rev. B. Phys.,* **80**, 3 (2009).

Received Nov. 28, 2019; Revised Jan. 8, 2020; Accepted Jan. 22, 2020

J. Magn. Soc. Jpn., **44**, 79-86 (2020)

<Paper>

Noise Suppression in Parallel Fluxgate Magnetometers by DC-Biased Excitation Method

D. Oyama, Y. Adachi, M. Miyamoto, N. Ono*, A. Imamura*, and D. Watanabe*

Applied Electronics Laboratory, Kanazawa Institute of Technology, *Amaike 3, Kanazawa, Ishikawa 920-1331, Japan*

*Sensors Department, Production Division, NEC Network and Sensor Systems, Ltd., *Asahimachi 7-1-1, Shiroishi, Miyagi, 989-0223, Japan*

We experimentally revealed that a direct current (DC) biased excitation method can reduce the noise in parallel fluxgate magnetometers composed of a permalloy ring core. The noise suppression was achieved by decreasing the Barkhausen noise and increasing the open-loop sensitivity using the nonlinearity of the *B-H* curve with the DC-biased excitation. The noise performance depends on the excitation parameters: frequency, amplitude, and DC-bias. We proposed that the parameters should be determined based on the evaluation of the sensitivity and noise level in both open-loop and closed-loop modes. Specifically, a contour map of the closed-loop noise is useful for understanding the noise decrease with different values of the amplitude and DC-bias. We also demonstrated the effectiveness of the DC-biased excitation method using a commercially available fluxgate magnetometer (APS520A, Applied Physics Systems). Using the DC-biased excitation method, the noise level was approximately one-fourth compared to that of the original electronics.

Key words: parallel fluxgate magnetometer, DC-biased excitation, noise suppression

1. Introduction

Fluxgate magnetometers are widely used in magnetic measurements, such as geomagnetic fields, magnetic exploration, magnetic metal detectors, buried objective surveying, and permeability measurements[1,2,3]. The advantage of the fluxgate magnetometer is that it can obtain high sensitivity from a direct current (DC) to several kHz bandwidth without any cryogenics.

The sensor heads of fluxgate magnetometers are usually composed of a core with an excitation coil and a sensing coil. The core is made of a soft magnetic material and excited by applying an alternative current (AC) magnetic field. High sensitivity can be achieved by detecting the modulated AC magnetic field corresponding to the external magnetic field via the sensing coil. There are two types of fluxgate magnetometers according to the direction of the magnetization of the core: parallel or orthogonal to the external magnetic field to be observed.

Sasada et al. developed an innovative orthogonal fluxgate magnetometer by applying a DC-biased excitation current to the amorphous wire and demodulating the detected signal using the fundamental frequency of excitation[4, 5]. The sensitivity (noise performance) of the fluxgate sensor was dramatically improved, and they successfully measured a magnetic signal from a human heart with 36 channel orthogonal fluxgate magnetometer array[6].

On the other hand, a low noise magnetic sensor named "differentially dc biased type magnetic field sensor" was proposed by Sonoda et al.[7, 8]. This sensor was composed of a pair of amorphous cores (wires or sheets) and its basic structure of the sensor head was same as the one of an amorphous core based parallel fluxgate magnetometer. The principle and optimization of excitation conditions were reported in 7) and 8).

Additionally, we found that the noise of the parallel fluxgate magnetometer composed of a permalloy ring could also be suppressed using a DC-biased excitation method, which applies the DC-biased excitation field to the core and demodulates the output signal of the sensing coil with the fundamental frequency, as based on Kado's idea[9]. We developed a multi-channel parallel fluxgate sensor array for a motion detector system using the DC-biased excitation method[10]. However, we have not yet confirmed that the noise can be suppressed by the DC-biased excitation method in parallel fluxgate magnetometers, although the basic concept of the sensor head are same as those of the previous studies. Therefore, the purpose of this paper is to reveal the effectiveness of noise suppression using the DC-biased excitation method in the permalloy ring core based parallel fluxgate magnetometer which has simple structure and is used widely compared with the amorphous core based sensors.

After describing the configuration of the fluxgate magnetometer and a setup for experiments in Section 2, we present our experimental results for revealing the mechanism and the effectiveness of the DC-biased excitation method in the parallel fluxgate magnetometer with the ring shaped permalloy core. In Section 3, the noise suppression mechanism is described. In Section 4, the optimization of the excitation parameters is discussed. In Section 5, we demonstrate the effectiveness of the DC-biased excitation method using a commercially available parallel fluxgate magnetometer.

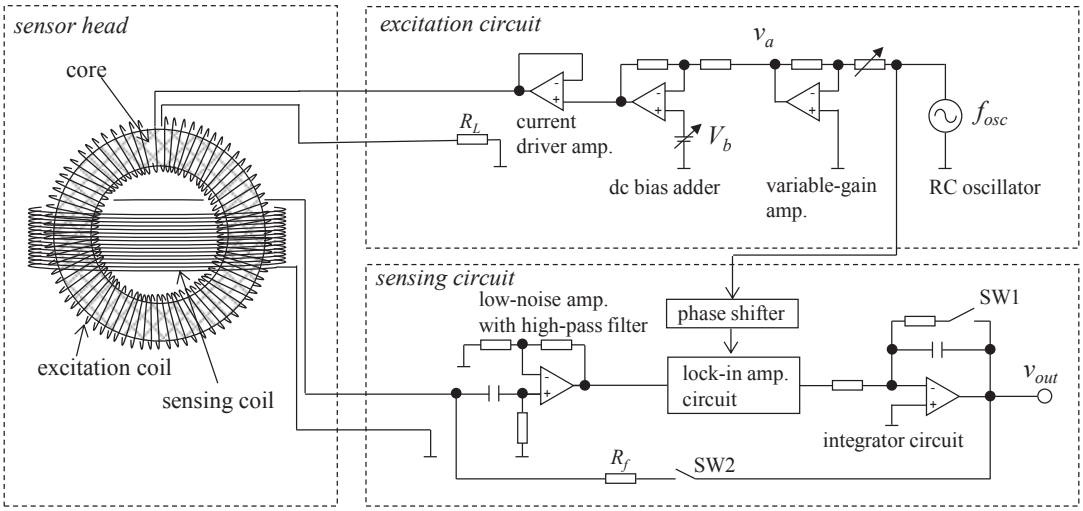

Fig. 1 Configuration of the fluxgate magnetometer.

2. Configuration of the Fluxgate Magnetometer and Experimental Setup

Figure 1 shows the configuration of our fluxgate magnetometer which is composed of a sensor head, an excitation circuit, and a sensing circuit. The ring-shaped magnetic core of the sensor head is made of permalloy and its thickness, inner- and outer-diameter are 0.3 mm, 13 mm, and 17 mm, respectively. The numbers of the excitation and sensing coils are 140 and 100, respectively.

The excitation circuit is composed of an RC oscillator, a variable-gain amplifier, a DC-bias voltage adder, and a current driver amplifier. The frequency of the output signal f_{osc} is determined by the combination of the resistor and the capacitor of the oscillation circuit. The oscillator outputs the sinusoidal waveform with the amplitude of approximately 1 V. The variable-gain amplifier is designed to increase from 0.1 to 10 so that the amplitude of the excitation signal (v_a) varies from 0.1 V to 10 V. The amplified sinusoidal waveform was biased by the DC voltage adder circuit. The DC bias voltage (V_b) is variable from −6 V to +6 V. The current driver amplifier is connected to the excitation coil of the sensor head. We used a high current operational amplifier (NJM4556AM, New Japan Radio Co., Ltd.), which can output up to ±70 mA, as the current driver amplifier.

The sensing circuit is connected to the sensing coil of the sensor head. Only the higher-frequency component of the sensing coil output is amplified by the low-noise amplifier (OP37, Analog Devices Inc.). The lock-in amplifier circuit is used to detect the magnetic signal applied to the sensor head from the modulated signal with the carrier frequency of f_{osc}. The reference signal of the lock-in amplifier is provided by the RC oscillator circuit, and its phase is tuned to maximize the open-loop sensitivity (OLS) in every measuring condition, which will be defined in the next section. The integrator and feedback circuit are used to linearize the input-output characteristics of the fluxgate magnetometer, which is also known as the null method. Two switches were inserted in the integrator and feedback circuits, which were used to evaluate the characteristics of the fluxgate sensors with the open-loop (SW1: close, SW2: open) and closed-loop (SW1: open, SW2: close) modes.

When the fluxgate magnetometer is operated in the closed-loop mode, the sensitivity coefficient (the input magnetic flux density of the sensor head vs. the output voltage of the sensing circuit) is fixed by the feedback resistor (R_f). We used a resistor of 1.1 kΩ for R_f, and the sensitivity coefficient was calibrated as 9.5 μT/V using the calibration method[11].

During experimental measurements, the sensor head is fixed to the center of a solenoid coil that is placed inside a magnetically shielded box (MSB) made of two layers of permaloy. The solenoid coil is connected to a function generator and applies a sinusoidal magnetic signal with a frequency of 8 Hz and an amplitude of 1.7 μT when measuring the input-output characteristics of the fluxgate magnetometer. The electronics including the excitation and sensing circuits were placed outside the MSB. The output signal of the sensing circuit is recorded by a 16-bit analog-to-digital converter after amplifying (variable gain) and low-pass filtering (500 Hz).

3. Experiments for Principle Verification

In this section, we show the possibility of noise suppression by applying a DC-biased excitation in parallel fluxgate magnetometers composed of the permalloy based ring core, and then we discuss its mechanism based on the sensor characteristics depending on the excitation.

3.1 Noise reducing effect by applying a DC-biased excitation

First, we experimentally confirmed that the

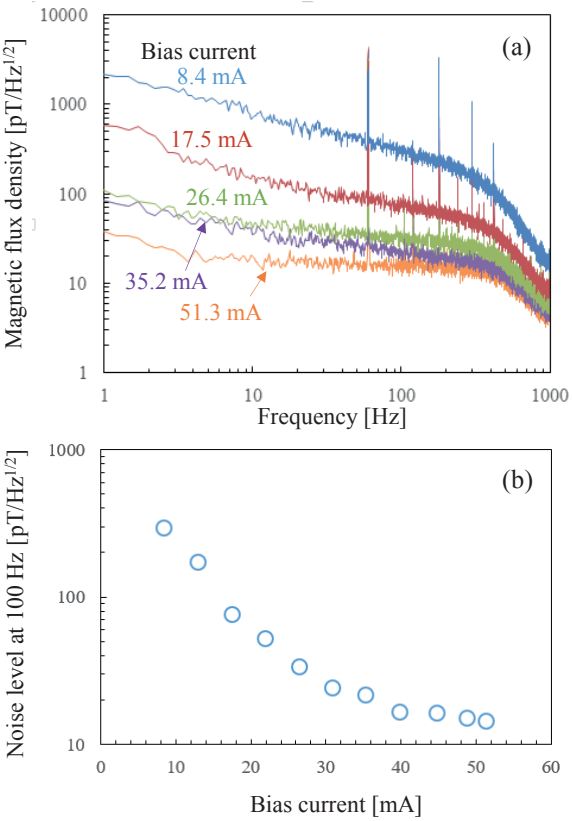

Fig.2 Noise level comparison between the DC-biases of the excitation. (a) Noise spectra and (b) noise level at 100 Hz.

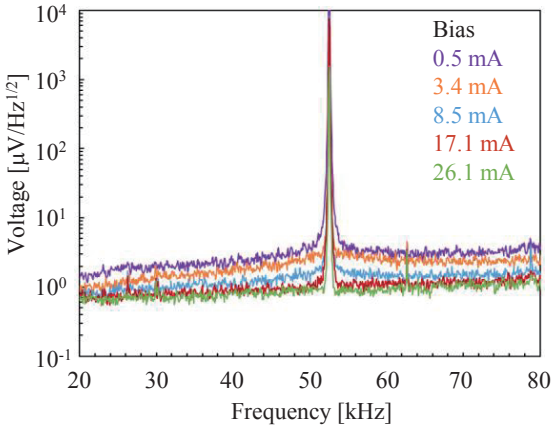

Fig.3 Open-loop noise (OLN) before lock-in detection.

DC-biased excitation method could suppress the noise of the parallel fluxgate magnetometer. We recorded the output signal v_{out} of the fluxgate magnetometer that operated in the closed-loop mode without applying the magnetic signal from the solenoid coil. Here, the excitation frequency f_{osc} and amplitude v_a were fixed to 53 kHz and 1.0 V, respectively (a comparison of different excitation frequencies and amplitudes will also be discussed later). Figure 2(a) shows the noise spectra when the fluxgate magnetometer was excited by different DC-bias currents and Fig. 2(b) plots the noise

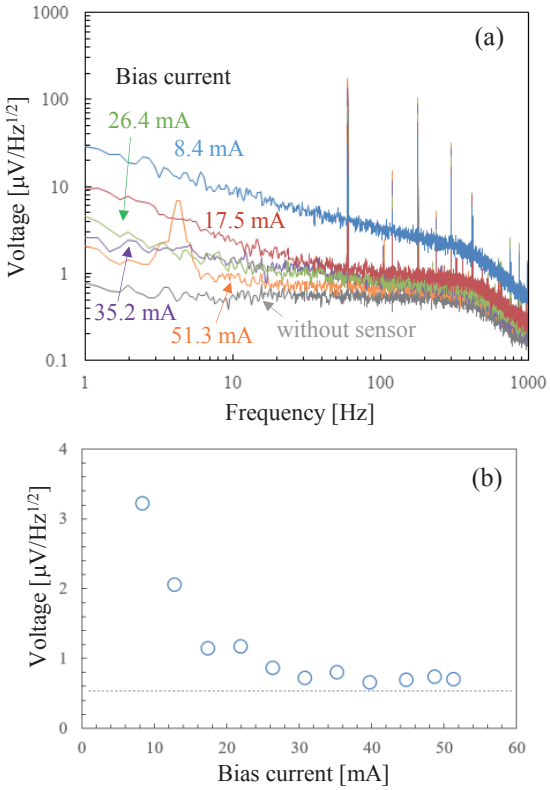

Fig. 4 OLN after lock-in detection. (a)Spectra and (b) noise level at 100 Hz.

level at 100 Hz. The noise floor decreases by increasing the DC-bias voltage for excitation. For example, the noise level was reduced to approximately 1/18 by increasing the bias voltage from 8.4 mA to 51.3 mA. The indicated values of the bias current were derived by measuring the voltage across the resistor R_L (110 Ω). These results clearly reveal that the DC-bias excitation method can reduce the noise of the parallel fluxgate magnetometer which is composed of a permalloy ring core and operated in the closed-loop mode.

3.2 Mechanism of reducing noise

In this subsection, we describe the mechanism of the noise suppression by investigating the characteristics of the sensor in the open-loop operation mode.

3.2.1 Noise performance in open-loop mode

In the orthogonal fluxgate sensors, reducing the Barkhausen noise by the DC-biased excitation is a main factor of the noise suppression[12]. To investigate the Barkhausen noise reduction in the parallel fluxgate, we measured the noise when the sensing circuit was operated in the open-loop mode. The excitation frequency and amplitude were fixed to 53 kHz and 1.0 V, respectively, and the DC-bias current was changed from 0.5 mA to 26.1 mA. Figure 3 shows the noise spectra of the output signal of the low-noise amplifier measured by a spectrum analyzer (35670A, Agilent Technologies). The largest peak at 53 kHz is the carrier signal with the excitation frequency f_{osc}. The noise floor level is suppressed by increasing the DC-bias current same as

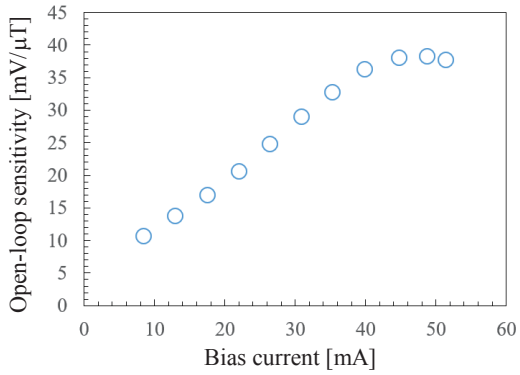

Fig. 5 Open-loop sensitivity (OLS).

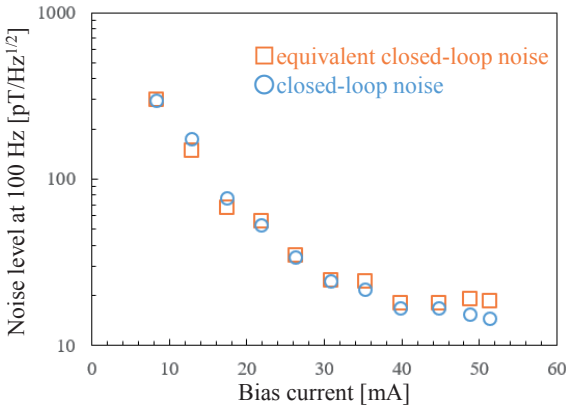

Fig. 6 Measured CLN (closed-loop noise, circle) and equivalent CLN (square) calculated from the OLN and OLS.

the result of the orthogonal fluxgate shown in 12). The Barkhausen noise is generated by randomly reversing the magnetic domain so that it appears when the the magnetization of the core is not saturated. The magnetization of the core is shifted to the saturation area by adding the DC-bias to the excitation current, therefore, the Barkhausen noise can be suppressed by the DC-biased excitation method.

Figure 4 shows the measured noise spectra of the output signal v_{out} of the fluxgate sensor operated in the open-loop mode with different DC-bias currents of the excitation. Because v_{out} is the demodulation signal of the output signal of the preamp, we assumed that the noise reduction (presented in Fig. 4(a)) was due to the suppression of the Barkhausen noise via increasing the DC-bias of the excitation. Here, a peak of approximately 4 Hz of the spectrum measured with the DC-bias of 51.3 mA was assumed to be caused by a vibration from the floor of the laboratory or MSB. The noise levels at 100 Hz are plotted in Fig. 4(b). The dashed line indicates the noise level of the sensing circuit measured without connecting the sensor probe. The noise decreasing below the bias current of 25 mA is due to the suppression of the Barkhausen noise as described in the previous subsection, and the circuit noise was dominant above 25 mA of the DC-bias current.

Here, the noise level reduction comparison between the DC-bias currents of 8 mA and 45 mA was about 1/5. This result cannot fully explain the noise level reduction of 1/18 when the fluxgate magnetometer was operated in the closed-loop mode. In addition to the noise spectrum, we evaluated the sensitivity for the open-loop operation mode to investigate the mechanism of the noise reduction in the closed-loop mode, as described in the next subsection.

3.2.2 Open-loop sensitivity

We measured the open-loop sensitivity (OLS) of the sensor. The sinusoidal magnetic signal was applied to the sensor and output voltage v_{out}, which was obtained by demodulation using the fundamental frequency of the excitation, was recorded. The OLS was derived by dividing the amplitude of v_{out} by the amplitude of the applied magnetic signal (1.7 μT).

The OLS measured with different DC-bias current is shown in Fig. 5. The OLS has a loose peak of around 45 mA. In principle, fluxgate magnetometers use the nonlinearity of the *B-H* curve of the core, therefore, the output signal of the sensing coil becomes the largest at the shoulder of the *B-H* curve. This result suggests that the magnetization of the core reaches the shoulder of the *B-H* curve by applying the DC-biased excitation current of 45 mA. The OLS, which corresponds to the output voltage of the sensing coil, can be maximized by adjusting the amount of the DC-bias of the excitation. Here, we should note that measuring OLS is the same approach as measuring the effective permeability reported in 7) and 8). We decided to evaluate the output voltage in open-loop mode operation in order to simplify the discussion to design the excitation parameters of the fluxgate magnetometers. This allows us to apply the DC-biased excitation method to unspecified sensor heads even if its structure is unknown as described in section 5.

3.3 Estimation of the closed-loop noise

Figure 6 shows the equivalent closed-loop noise (CLN) calculated as

$$Equivalent\ CLN\ [\mathrm{pT/Hz^{1/2}}] = (OLN\ [\mathrm{\mu V/Hz^{1/2}}] / OLS\ [\mathrm{mV/\mu T}]) \times 10^{-3} \quad (1),$$

where OLN and OLS are the noise level and sensitivity in the open-loop operation, respectively. The measured CLN is also plotted in Fig. 6 (same data as Fig. 2(b)), and the data is in accordance with the equivalent CLN. The noise level of the fluxgate magnetometer, which is usually operated in the closed-loop mode, was determined based on both the noise level and sensitivity in the open-loop operation mode in the same as the differentially dc biased type magnetic field sensor. Therefore, we concluded that the noise suppression by the DC-biased excitation method was due to two factors: decreasing the Barkhausen noise and increasing the sensitivity using the nonlinearity of the *B-H* curve.

4. Optimization of the Excitation Parameters

The results shown in previous section were measured with the fixed amplitude v_a and frequency f_{osc} of the excitation to 1.0 V and 53 kHz, respectively. In this

section, we present the results of the sensor characteristics measurements and discuss how to choose the optimal excitation parameters.

4.1 Excitation frequency

We measured the OLS, OLN, and CLN with different excitation frequencies of 26 kHz, 78 kHz, and 103 kHz, respectively. The amplitude of the excitation was fixed to 1.0 V in the same manner as the experiment described in the previous section. Figure 7 shows the results with a changing DC-bias voltage in each excitation frequency. The results with 53 kHz are the same data plotted in Figs. 2(b), 4(b), and 5.

As shown in Fig. 7(a), the OLS was proportional to the square root of the excitation frequency, although the sensitivity of the sensing coil is theoretically proportional to the frequency. The effective area of the cross-section of the core is proportional to the reciprocal of the square root of the frequency due to the skin effect. The results suggested that the OLS was proportional to the square root of the excitation frequency $f_{osc}^{1/2}$ as the product of the sensitivity of the sensing coil (proportional to f_{osc}) and the effective area of the cross-section of the core (proportional to $f_{osc}^{-1/2}$).

Conversely, the OLN slightly increased with a higher excitation frequency. Potential white noise sources may have existed during this experiment, such as the Barkhausen noise and thermal noise of the sensing coil. These white noise appeared as a frequency proportional noise as shown in Fig. 3 because the induced electromotive force of the sensing coil is proportional to the signal frequency.

Consequently, suppression of the CLN via the DC-biased excitation method was evenly achieved with the excitation frequencies of 53 kHz, 78 kHz, and 103 kHz, but the suppression result with 26 kHz was slightly larger than others, as shown in Fig. 7(c). We observed that the improvement of the CLN is not proportional to the excitation frequency, so we had to consider both the OLS and the OLN to decide the excitation frequency.

To show additional criteria needed to choose the excitation frequency, we measured the frequency response when the DC-bias voltage was fixed to approximately 45 mA and the sensor circuit was operated in the closed-loop mode. The frequency response was measured using a frequency response analyzer (FRA5097, NF Corporation). The measured frequency responses are plotted in Fig. 8. The bandwidth (frequency at which the response is −3 dB) became wider by increasing the excitation frequency. In general, the bandwidth of the closed-loop feedback system is proportional to the open-loop gain of the system. In the case of the developed fluxgate magnetometer, the OLS corresponded to the open-loop gain of the feedback; therefore, the bandwidth of the sensor was expanded corresponding to increase in the excitation frequency.

Based on the results of the CLN and frequency response, we decided to set an excitation frequency of 103 kHz to obtain both the low CLN and wide bandwidth.

4.2 Excitation amplitude

After choosing the excitation frequency of 103 kHz, we compared the sensor characteristics with different

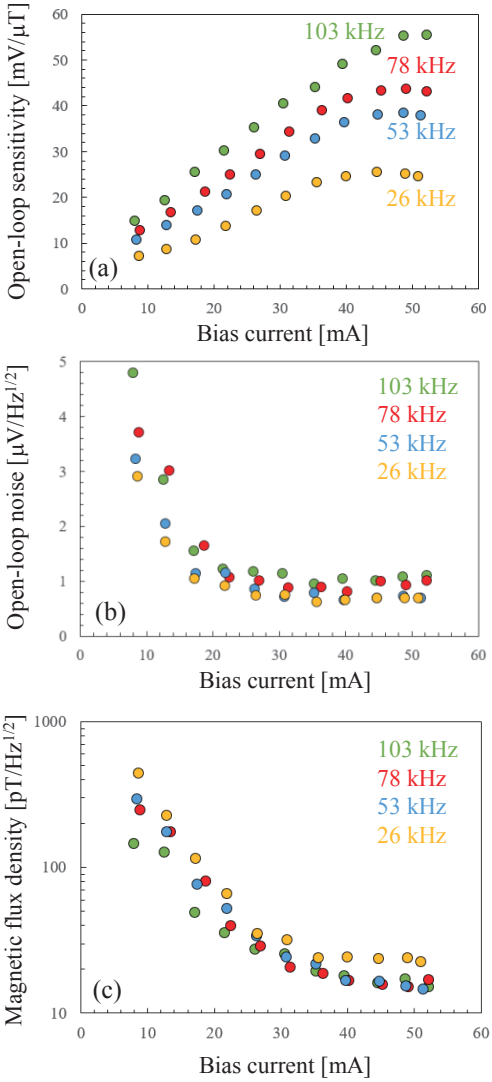

Fig. 7 Comparison of the excitation frequency. (a) OLS, (b) OLN, and (c) CLN.

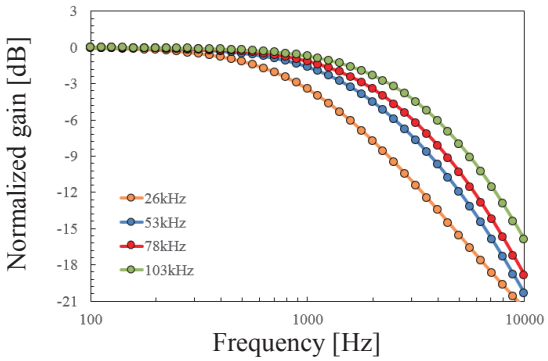

Fig. 8 Frequency response comparison between the excitation frequency.

excitation amplitude (indicated as v_a in Fig. 1) of 0.5 V, 1.0 V, 1.5 V, and 2.0 V. In this experiment, we measured the amplitude of the excitation current as shown in Fig. 9. Although v_a was fixed in each

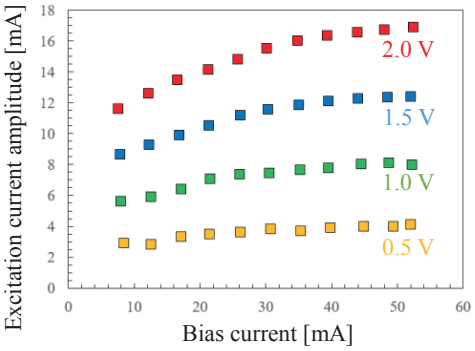

Fig. 9 Dependence of excitation current amplitude on the applied voltage and the DC-bias current.

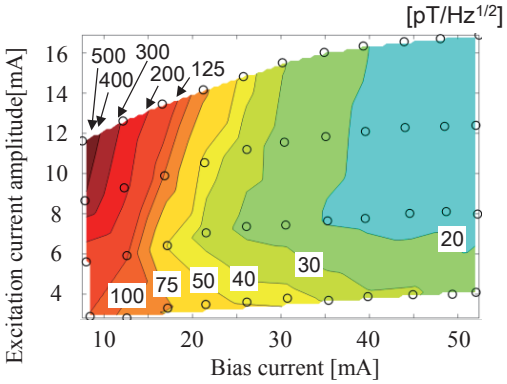

Fig. 11 Contour graph of the closed-loop noise.

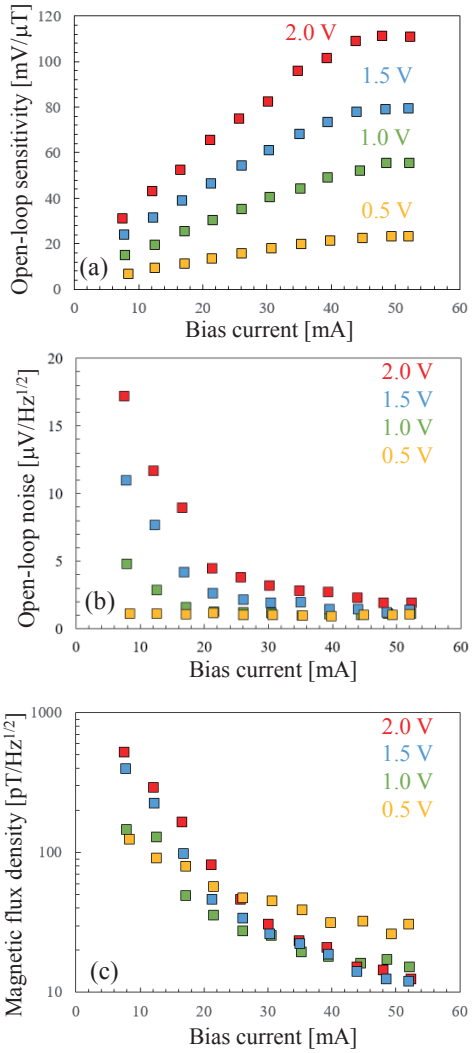

Fig. 10 Comparison of the excitation amplitudes. (a) OLS, (b) OLN, and (c) CLN.

measurement, the current amplitude slightly changed according to the bias current. This result shows that the permeability of the core changed according to the bias current because the impedance of the excitation coil is proportional to the permeability of the core. These curves became almost flat above approximately 45 mA of the bias current, therefore, this result also supports that the magnetization of the core reached the shoulder of the *B-H* curve by applying the DC-biased excitation current of 45 mA as described in section 3.2.

Figure 10 shows the OLS, OLN, and CLN with changing DC-bias current in each excitation amplitude. The results with 1.0 V are the same data as those plotted in Figs. 2(b), 4(b), and 5.

Both the OLS and the OLN increased with the enlarged amplitude of the excitation signal. The OLS was proportional to the excitation amplitude; in contrast, the OLN showed a lower decrease limit. The convergence value was approximately the same as the noise level that originated from the electronics shown in Fig. 4(b). As plotted in Fig. 10(c), the measured CLN was suppressed by increasing the DC-bias voltage and appeared to be a function of both the DC-bias and amplitude of the excitation.

To facilitate the optimization of the DC-bias and amplitude of the excitation, we visualized the measured CLN, which is plotted in Fig. 10(c), as a contour graph in Fig. 11. The excitation current amplitude in the vertical axis was derived from the plots in Fig. 9. According to this contour graph, choosing large values for both amplitude and DC-bias achieves the noise suppression in the fluxgate sensor; for example, a noise level of less than 20 pT/Hz$^{1/2}$ was obtained when the excitation amplitude and bias were set to the values included in the blue area.

When designing the fluxgate magnetometer in practice, there must be limitations to the electronics, such as power consumption and the slew rate of the current driver. We can choose the optimal excitation parameters for variable applications by referring to the experimentally obtained contour map of the CLN.

5. Demonstration Using a Commercially Available Fluxgate Sensor

We experimentally compared the noise performance between the conventional sensing and DC-biased excitation method to demonstrate the effectiveness of

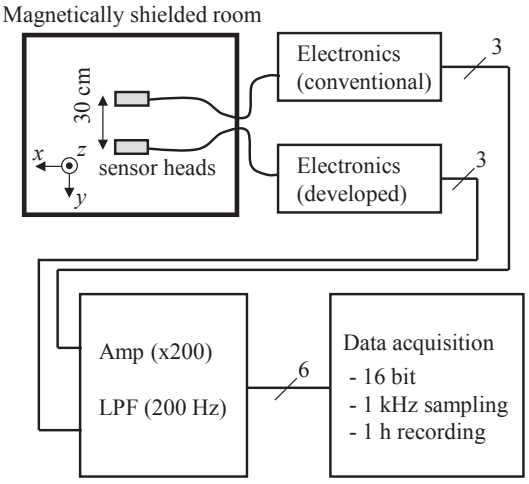

Fig. 12 Block diagram of the comparative experiment

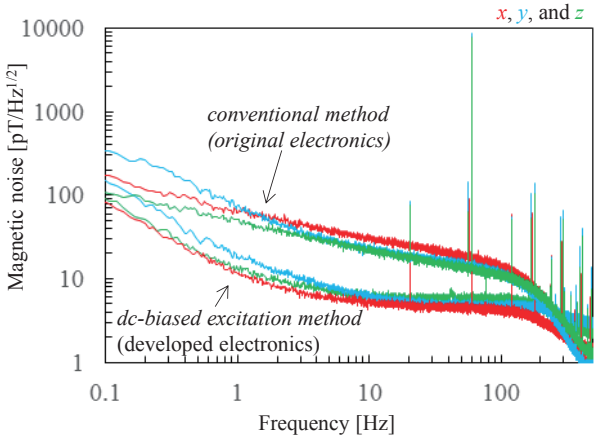

Fig. 13 Noise comparison between conventional and developed circuit.

the DC-biased excitation method. We used two sets of a commercially available fluxgate magnetometer (APS520A, Applied Physics Systems). This fluxgate magnetometer has three orthogonally arranged ring-shaped sensor heads made of supermalloy in a single probe, which is operated by conventional method with the excitation frequency of 25 kHz[13].

Figure 12 shows the block diagram of the experiment. Two APS520A sensor probes were placed in a magnetically shielded room composed of two layers of permaloy and single layer of cupper. One of the probes was connected to the original electronics of APS520A, and another one was connected to our electronics to operate with the DC-biased excitation method. We customized the electronics to have three-channel sensing circuits and a single-channel excitation circuit. We observed that the excitation coils of each core are connected in the sensor probe. Although the details of the connection in the probe were not available due to the confidentiality policy of Applied Physics Systems, we decided to supply the excitation signal from a single-channel excitation circuit. The frequency, amplitude, and DC-bias were fixed to 103 kHz, 8.1 mA and 19.5 mA, respectively, after evaluating the CLN with different excitation conditions.

The output signals of both fluxgate sensors were simultaneously recorded by a data acquisition system via amplifiers (200 of gain) and low-pass filters (200 Hz of cutoff frequency).

Figure 13 shows the measured noise spectra of all outputs. The noise floor measured with the DC-biased excitation method is smaller than the floor measured with the original electronics. For example, the mean values of the three channels at 5 Hz and 100 Hz measured with the DC-biased excitation and conventional methods were 7.2 and 31.6 pT/Hz$^{1/2}$, 4.9 and 12.2 pT/Hz$^{1/2}$, respectively. We concluded that the DC-biased excitation method is effective in suppressing the noise of parallel fluxgate magnetometers.

6. Discussion

In this paper, we revealed the effectiveness of noise suppression using the DC-biased excitation in the parallel fluxgate magnetometers composed of permalloy based ring core. As demonstrated in section 5, this technique is effective even for existing sensor head which was originally designed for the conventional excitation. Many parallel fluxgate magnetometers have been developed so far, as introduced in 1), 2), and 3). Recently, Miles et al.[14] developed low-noise permalloy ring cores for parallel fluxgate magnetometers which achieved noise level of 6 to 11 pT/Hz$^{1/2}$. There is a possibility to reduce the noise level of those sensors using the DC-biased excitation method. Moreover, there also is a possibility to achieve much lower noise level by optimizing the structure of the sensor head, including the core, the excitation coil, and the sensing coil, for the DC-biased excitation method. Approaching the noise level of sub-pT/Hz$^{1/2}$ like the amorphous core based sensors[4-8] is the topic of our further study.

Additionally, magnetic offset should be considered in fluxgate magnetometers. Unbalance of magnetization in the core often causes unexpected offset in the output signal[15]. In case of the DC-biased excitation method, the unbalance of magnetization results in larger offset due to the DC-bias current. The magnetic offset can easily be compensated by adding the DC-current to the sensing coil in parallel to the feedback signal. Description of the offset compensation circuit was omitted to focus on the noise suppression in the fluxgate magnetometer.

7. Conclusion

In this study, we detailed the mechanism and effectiveness of the DC-biased excitation method for noise suppression in parallel fluxgate magnetometers.

We also revealed that the noise suppression was caused by both decreasing the Barkhausen noise and increasing the OLS using the nonlinearity of the *B-H* curve with the DC-biased excitation. The noise level was strongly dependent on the excitation conditions, especially the amplitude and DC-bias. The visualization of the CLN using the contour map provided a suitable combination of the excitation amplitude and DC-bias.

As demonstrated in Section 5, the DC-biased excitation method is applicable for existing parallel fluxgate magnetometers when changing the electronics. We believe that the DC-biased excitation method and its design described in this paper are not only effective for potentially developing a new magnetometer but can also be useful in improving the noise performance of conventional parallel fluxgate magnetometers composed of permalloy ring cores.

Acknowledgements The authors would like to thank the late Professor Hisashi Kado, whose leadership provided valuable guidance. We would like to thank Editage (www.editage.com) for English language editing. The authors wish to thank the anonymous reviewers for their valuable comments.

References

1) K. Mori: Magnetic Sensors (Augmented edition) —From Principles of Sensors to Applications of Electronic Compass— (in Japanese), p. 80 (Corona Publishing Co., Ltd., Tokyo, 2016).
2) S. Yabukami: *Magn. Jpn.*, **11**, 156 (2016).
3) N. Nishimura and M. Takahata: *Magn. Jpn.*, **12**, 126 (2017).
4) I. Sasada: *J. Appl. Phys.*, **91**, 7789 (2002).
5) I. Sasada: *Magn.Jpn.*, **14**, 205 (2019)
6) H. Karo, K. Shimoda, Y. Maeda, and I. Sasada: *IEEJ Trans. Sens. Micromachines*, **136**, 224 (2016).
7) T. Sonoda, R. Ueda, H. Ikemoto, K. Kudo, K. Kajiwara: *IEEE Trans. Magn.*, **25**, 3396 (1989).
8) T. Sonoda, H. Azuma, T. Matsuo: *T. IEE Japan*, **120-A**, 322 (2000).
9) H. Kado: Japanese Patent, No. 3651268.
10) D. Oyama, Y. Adachi, M. Higuchi, and G. Uehara: *IEEE Trans. Magn.*, **50**, 5101604 (2014).
11) T. Yoshida, M. Higuchi, T. Komuro, and H. Kado: *Proc. 16th Annu. Int. Conf. IEEE Eng. Adv.: New Opportunities Biomed. Eng.*, 171 (1994).
12) E. Paperno: *Sens. Actuators*, **A 116**, 405 (2004).
13) *APS520/520A 3 Axis Fluxgate Magnetometer Operating Manual and Technical Reference*, Applied Physics Systems (1996).
14) D. M. Miles, et al.: *Geosci Instrum, Method. Data Syst.*, **8**, 227 (2019).
15) G. Musmann, Y. Afanassiev: Fluxgate Magnetometers for Space Research, pp. 73-112 (Books on Demand GmbH, Norderstedt, 2010).

Received Jan. 14, 2020; Revised Feb. 25, 2020; Accepted Mar. 11, 2020

Journal of the Magnetics Society of Japan

Vol. 44 No. 3 (通巻第 309号) 2020年5月1日発行

Vol. 44 No. 3 Published May 1, 2020
by the Magnetics Society of Japan
Tokyo YWCA building Rm207, 1–8–11 Kanda surugadai, Chiyoda-ku, Tokyo 101–0062
Tel. +81–3–5281–0106 Fax. +81–3–5281–0107

Printed by JP Corporation Co., Ltd.
Sports Plaza building 401, 2–4–3, Shinkamata Ota-ku, Tokyo 144–0054
Advertising agency: Kagaku Gijutsu-sha

発行：（公社）日本磁気学会 101–0062 東京都千代田区神田駿河台 1–8–11 東京YWCA会館 207 号室
製作：ジェイピーシー 144–0054 東京都大田区新蒲田 2–4–3 スポーツプラザビル401 Tel.（03）6715–7915
広告取扱い：科学技術社 111–0052 東京都台東区柳橋 2–10–8 武田ビル 4F Tel.（03）5809–1132